

# Elucidating the control and development of skin patterning in cuttlefish

Sam Reiter<sup>1</sup>, Philipp Hülsdunk<sup>1,2</sup>, Theodosia Woo<sup>1</sup>, Marcel A. Lauterbach<sup>1</sup>, Jessica S. Eberle<sup>1</sup>, Leyla Anne Akay<sup>1</sup>, Amber Longo<sup>1</sup>, Jakob Meier-Credo<sup>1</sup>, Friedrich Kretschmer<sup>1</sup>, Julian D. Langer<sup>1,3</sup>, Matthias Kaschube<sup>2</sup> & Gilles Laurent<sup>1\*</sup>

Few animals provide a readout that is as objective of their perceptual state as camouflaging cephalopods. Their skin display system includes an extensive array of pigment cells (chromatophores), each expandable by radial muscles controlled by motor neurons. If one could track the individual expansion states of the chromatophores, one would obtain a quantitative description—and potentially even a neural description by proxy—of the perceptual state of the animal in real time. Here we present the use of computational and analytical methods to achieve this in behaving animals, quantifying the states of tens of thousands of chromatophores at sixty frames per second, at single-cell resolution, and over weeks. We infer a statistical hierarchy of motor control, reveal an underlying low-dimensional structure to pattern dynamics and uncover rules that govern the development of skin patterns. This approach provides an objective description of complex perceptual behaviour, and a powerful means to uncover the organizational principles that underlie the function, dynamics and morphogenesis of neural systems.

Cuttlefish and octopuses have an unmatched ability to change their external appearance for camouflage or communication<sup>1</sup>. When camouflaging, they produce a statistical approximation of their visual environment following rules that remain unknown. Because cephalopod camouflage appeared evolutionarily as a response to predators and because their performance can fool humans as well, the rules of pattern generation that they express may be instructive to the texture perception across animals, and reveal biological solutions to a general problem of computational vision and neuroscience<sup>2–6</sup>.

Since pioneering work on cephalopod chromatophores in the 1960s<sup>7,8</sup>, several groups have revealed the remarkable complexity of this system<sup>9–11</sup>. Pigment-carrying chromatophores—the pixels of this two-dimensional texture generation system—expand and contract in direct response to the activity of motor neurons<sup>8</sup>, which project from the brain<sup>12</sup> and make excitatory glutamatergic synaptic connections<sup>13</sup> with sets of muscles that are arranged radially<sup>14</sup>. Chromatophores operate in concert with other specialized cells (for example, leucophores and iridophores) and dermal muscular systems to generate a rich array of coordinated textures, dynamic patterns and behaviours.

The rules of neural control governing this system remain largely unknown, owing mostly to the challenges of tracking large numbers (thousands to millions) of small (15–100-μm diameter) chromatophores in soft-bodied, behaving animals. Because each chromatophore is controlled by a small number of motor neurons and conversely, because each motor neuron controls a small number of chromatophores (its motor unit)<sup>12,14,15</sup>, we reasoned that chromatophore expansion could serve as a proxy for motor neuron activity. Analysis of the joint statistics of chromatophore variation might in turn reveal the structure of a hypothetical control hierarchy. This study presents our solutions to this challenge, a method for tracking nearly all chromatophores of the dorsal mantle of a cuttlefish at a high frame rate and over developmental timescales. Using this technique, we take the first quantitative steps towards elucidating the control, dynamics and morphogenesis of this system.

## Tracking chromatophores in freely behaving animals

Freely behaving animals were filmed in a tank with variable backgrounds (Methods). Our first goal was to segment all visible chromatophores in all images and then align these images by mapping them into a common reference frame (Fig. 1a). In any recording session, continuous image sequences with the animal in view and in focus ('chunks', Fig. 1b) were interspersed by unusable periods of movement (grey, Fig. 1b). Chunks were selected post hoc using a statistic of focus (Fig. 1b and Methods). Within a chunk, the pixels of each frame were first classified<sup>16</sup> as belonging either to a chromatophore (of any colour) or to background (Fig. 1c, Extended Data Fig. 1 and Methods). All frames in one chunk were mapped into a common reference frame using sparse optical flow<sup>17</sup> (Fig. 1d and Supplementary Video 1) and averaged into one 'master frame' (Fig. 1e, top row, left and middle).

To track individual chromatophores across filming gaps, we stitched chunks together. By correlating a small patch of skin (purple and green frames, Fig. 1e) within one master frame with all possible positions and orientations of identically sized patches in another master frame, a single 'fingerprint' match was usually detected (see two-dimensional correlations in Fig. 1e, note the sensitivity to small shifts in the bottom left panel; see also Extended Data Fig. 2). We used a matching procedure over a grid of patches (Fig. 1e, top left and bottom right, red), interpolating between matching points, to map all master frames into a common reference frame (Methods and Supplementary Video 2). Over 970 analysed master frames, 85% had an average mapping error of  $\leq 3$  pixels per  $20 \pm 6 \mu\text{m}$ . The following data come from 1,178,146 mapped frames, from six animals.

Averaging all aligned master frames in a dataset produced a single 'queen frame'. Using local maxima, we partitioned the queen frame into non-overlapping sectors, each representing the space that a single chromatophore can occupy (Fig. 1f). The number of chromatophore pixels in each sector was then used to quantify the expansion state of the corresponding chromatophore in each image of the dataset (Fig. 1g). We thus obtained tens of thousands of parallel and simultaneous chromatophore–activity times series, characterizing skin patterns and their evolution (Methods).

<sup>1</sup>Max Planck Institute for Brain Research, Frankfurt am Main, Germany. <sup>2</sup>Frankfurt Institute for Advanced Studies and Department of Computer Science and Mathematics, Goethe University, Frankfurt am Main, Germany. <sup>3</sup>Max Planck Institute of Biophysics, Frankfurt am Main, Germany. \*e-mail: gilles.laurent@brain.mpg.de

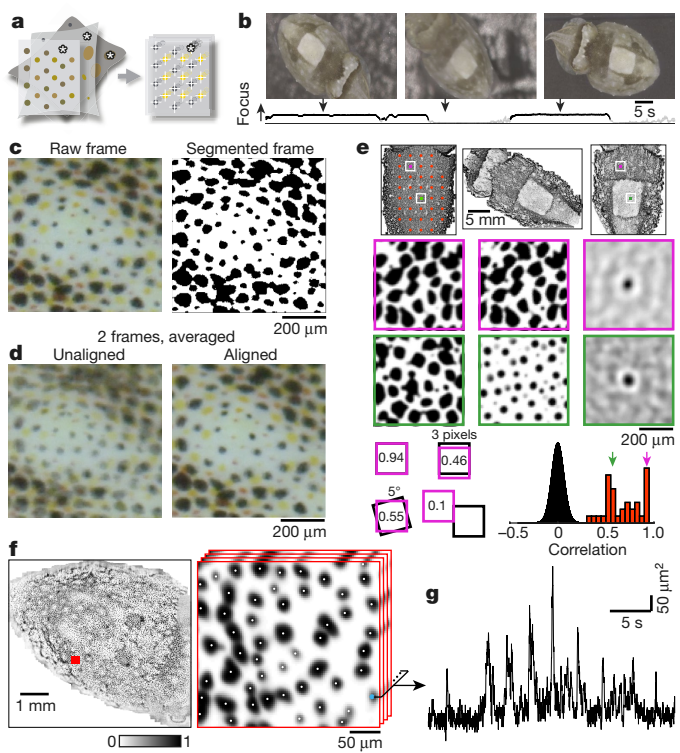


**Fig. 1 | Chromatophore tracking in behaving cuttlefish.** **a**, Schematic of approach to track the expansion state of many single, identified chromatophores over time through nonlinear image alignment. An example chromatophore is indicated by an asterisk. **b**, Data acquisition. ‘Chunks’ of in-focus image segments are identified with a focus statistic (black, bottom), separated by out-of-focus segments (grey). **c**, Segmentation. Pixels are classified as belonging either to a chromatophore (black, right) or to background (white). **d**, Alignment. Compare the averages of two frames with and without within-chunk alignment. **e**, Stitching. Top row, one master frame (middle) is mapped into the reference frame of another (left), resulting in the image on the right. Middle two rows, corresponding patches of skin (purple and green dots in the top images), after alignment (left and middle). Matches were made possible by the peak in spatial cross-correlation function (right) even when chromatophore states differ (green). Bottom row, left, shifting or rotating corresponding patches (purple frame) rapidly decreases correlation (Pearson’s correlation). Bottom row, right, distribution of correlation values of  $64 \times 64$ -pixel skin patches (as above) across aligned master frames at all translations (sampled every pixel) and rotations (sampled every  $60^\circ$ ). Correct matches (red):  $n = 36$ . Non-matching pairings (black),  $n = 485,722,908$ . **f**, Defining chromatophores. Left, queen frame ( $n = 167,065$  aligned, averaged, segmented frames). Right, zoom-in of the red square on the left; single-chromatophore centres indicated with white dots. **g**, Raw expansion state of chromatophore in **f** (blue) over successive frames.

### Classifying chromatophores by colour

Cuttlefish chromatophores come in different colours (Fig. 2a), which are usually classified in 3–5 groups<sup>9,18,19</sup>. To characterize chromatophore colour objectively, we measured their transmission spectra in freshly dissected skin (Fig. 2b and Methods). The distribution of spectra at 615 nm was bimodal, with a ‘dark’ and a ‘light’ cluster, plus intermediate colours ranging from orange to red. This could be explained in part by expansion state: local application of L-glutamate<sup>13</sup>—which induces chromatophore expansion—caused spectral changes towards lighter colours (Extended Data Fig. 3), consistent with previous descriptions<sup>20,21</sup>, and possibly explained by decreased local density and nano-structural features of the pigment granules<sup>22</sup>. Using mass spectrometry-based techniques, we identified xanthommatin as a pigment in *Sepia* skin, and localized it exclusively to light chromatophores (Extended Data Fig. 3). Therefore, we can segregate chromatophores of *Sepia officinalis* into two groups (light and dark) defined, respectively, by the presence and absence of xanthommatin. This confirms our initial classification based on transmission spectra (Fig. 2b).

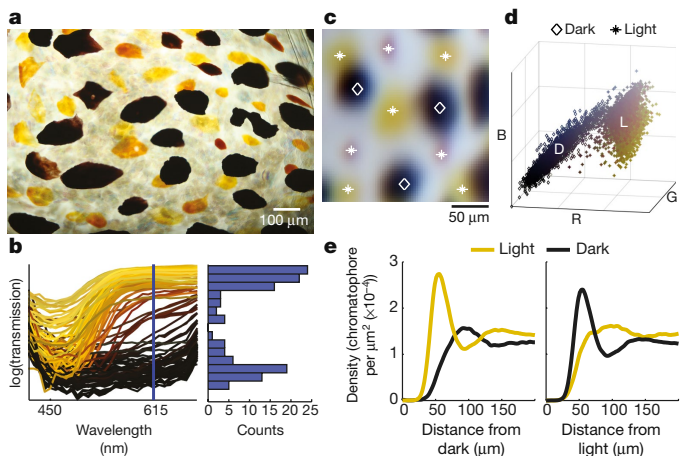


**Fig. 2 | Classifying chromatophores by colour.** **a**, Isolated skin sample illustrating range of chromatophore colours. **b**, Transmission spectra of chromatophores, including those shown in **a**. Lines correspond to regions of interest of individual chromatophores, coloured as the average RGB value for that region of interest. Right, frequency distribution histogram for transmission at 615 nm. **c**, Small patch of averaged, aligned colour images ( $n = 28,998$  frames) showing dark (diamond) and light (star) colour assignments. **d**, Normalized RGB colour distribution for pixels centred on  $n = 9,199$  chromatophores on the mantle of one animal. Symbols as in **c**. **e**, Radial-averaged density of light and dark chromatophores centred on dark (left) and light (right) reference chromatophores.  $n = 11,535$  dark; 14,802 light chromatophores, from three animals.

Consistent with results *in vitro*, chromatophore colour *in vivo* defined two modes, with partially overlapping dark and light (yellow to brown) clusters (Fig. 2c, d and Methods). The spatial arrangement of chromatophore colour was not random (Fig. 2e): we calculated the average local density of each colour class centred on chromatophores of a single colour (Fig. 2e; 32,740 chromatophores, three animals; Methods). On average, chromatophores of either class occupied an approximately 20-µm radius area. Beyond this, the density of opposite-colour chromatophores increased and dominated, peaking at around 55 µm. At about 100 µm, colour densities were inverted, indicating an alternation (on average) between light and dark chromatophores (see also Extended Data Fig. 4).

### Decomposing chromatophore control

To infer the potential structure of the control circuitry of the chromatophores, we examined their temporal co-variation during spontaneous fluctuations *in vivo*. This analysis is complicated by the fact that each chromatophore may be innervated multiple times and the possibility that individual motor units may overlap<sup>14,23–28</sup> (Extended Data Fig. 5).

To identify motor units directly, we first carried out minimal electrical stimulation of distal nerve branchlets that innervate freshly dissected dorsal mantle skin and measured resulting chromatophore expansion (Methods). Putative motor units were small (2–10 chromatophores), usually clustered (median radius of 2.5 chromatophores or 247 µm) and monochromatic (Fig. 3a and Extended Data Fig. 5), consistent with observations in squid and octopuses<sup>12,21,27,28</sup>. Light motor units were harder to stimulate electrically in isolation than dark ones, suggesting smaller axons.

Close observation of behaving animals revealed pronounced coordinated fluctuations of small localized groups of chromatophores, suggesting common drive (Supplementary Video 3). Seeking to extract these groups statistically, we factorized the chromatophore activity matrix using independent component analysis<sup>29,30</sup> and clustered through thresholding chromatophores that contributed strongly to single independent components, allowing for multiple-cluster membership (Methods). We called these inferred clusters of chromatophores ‘motor elements’ to distinguish them from anatomically defined motor units (see above).

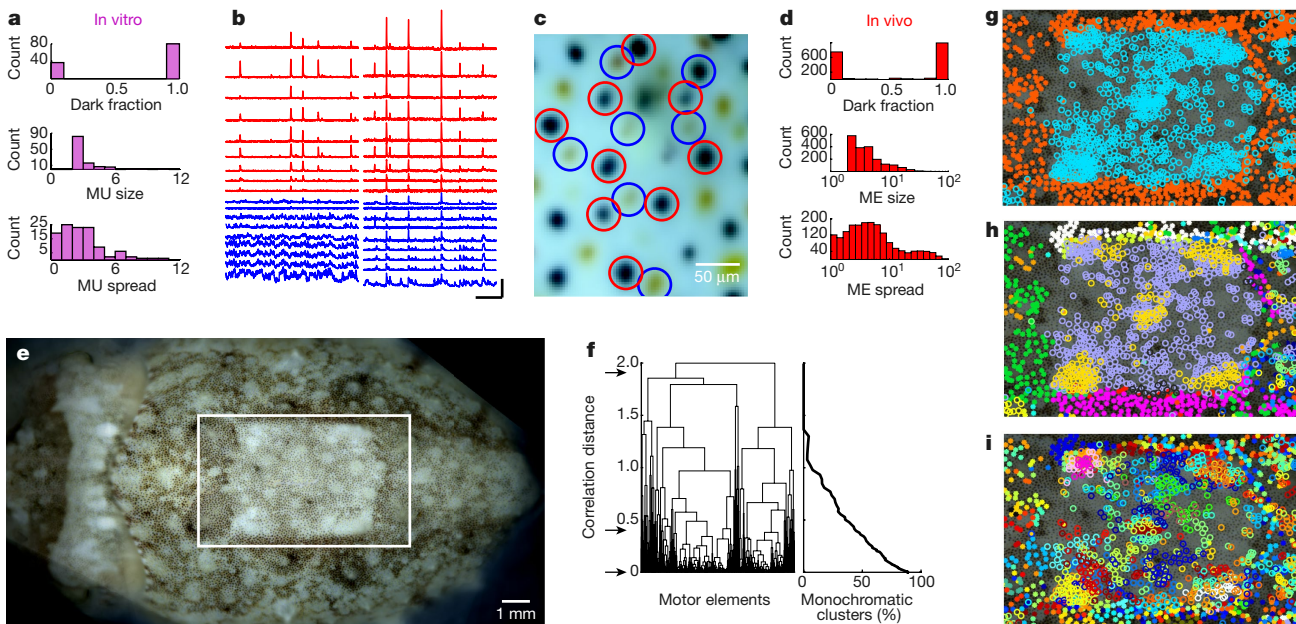


**Fig. 3 | Inferring chromatophore neural control from co-variation.**

**a**, Summary statistics of in vitro experiments. Top, fraction of dark chromatophores in a motor unit (MU). Middle, number of chromatophores in a motor unit. Bottom, average distance to motor unit centroid for all chromatophores in that motor unit, normalized to the average nearest-neighbour distance over all chromatophores ( $n = 295$  chromatophores, 114 motor units). **b**, Identification of motor elements (MEs) in vivo. Size-over-time traces for 18 chromatophores over two chunks. Red, nine chromatophores clustered as one motor element. Blue, nearest neighbours (in physical space) to the chromatophores in red.

Calibrations:  $x = 5$  s;  $y = 1,000 \mu\text{m}^2$ . **c**, Average colour image showing position and colour of chromatophores in **b** (circles, colours). **d**, Summary statistics of in vivo experiments. Compare to **a**. **e**, Aligned colour image showing ‘average’ pattern over an approximately 1 h-long dataset (237,826 frames). **f**, Left, correlation-based hierarchical clustering of average motor element time courses for the dataset in **e** ( $n = 695$  motor elements). Right, fraction of monochromatic clusters as a function of correlation distance ( $n = 1,896$  motor elements, 3 animals). **g–i**, Clusters at threshold levels in **f** (arrows, top to bottom) within frame in **e**. Same symbols throughout; colours denote cluster identities.

Using  $57 \pm 10$ -min-long datasets, we extracted hundreds of motor elements across the mantle of an animal. Although chromatophores within a motor element tended to be highly correlated with each other, we often observed subsets within a motor element that occasionally fluctuated independently of the others. We also regularly saw transient co-fluctuations with unclustered, otherwise weakly correlated, chromatophores (Fig. 3b).

Motor elements were mostly monochromatic (89% contained only light or dark) and their size distribution was heavy-tailed, with a

median of three chromatophores (Fig. 3d and Extended Data Fig. 5). Note that their size distribution resembles that of presumed motor units (Fig. 3a, d)—with the tail likely to represent groups of highly coordinated motor units, identified by independent component analysis. Chromatophores within a motor element were typically clustered physically, but were usually not ‘nearest neighbours’, consistent with colour alternation (Fig. 2e) and monochromativity. The distribution of spatial clustering was also heavy-tailed, with few motor elements containing chromatophores spread over large areas (Fig. 3d).

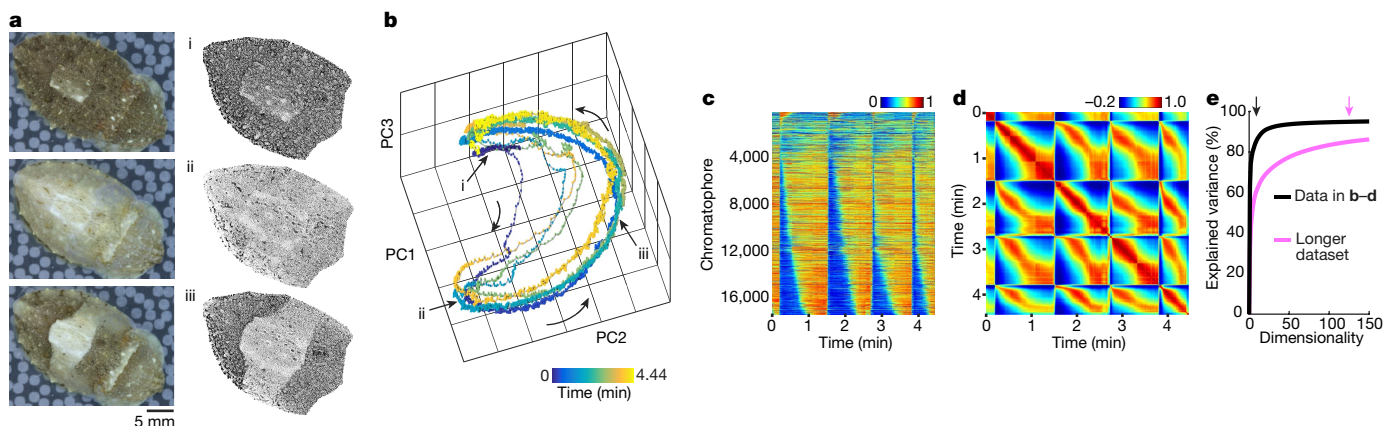


**Fig. 4 | Tracking pattern changes at cellular resolution.** **a**, Snapshots (i–iii) of an animal reacting to motion. Left, raw images. Right, corresponding segmented images: chromatophores are shown as disks proportional to actual size ( $n = 17,305$  chromatophores, see Supplementary Video 5). **b**, Full sequence of skin patterns (17,305-dimensional vectors of chromatophore sizes, unfiltered) over repeats of the behaviour, projected into space of the first three principal components (PC1–PC3). Time is shown in colour. **c**, Full area-over-time matrix of the behavioural

sequence in **b**. Chromatophore areas normalized for visualization (0–1) and ordered by time-to-cross mean activity during first sequence (15–88 s). **d**, Correlation matrix of full, 17,305-dimensional vectors of chromatophore sizes (Pearson’s correlation). **e**, Cumulative variance explained by increasing numbers of principal components (dimensions). Black, sequence in **b–d**; magenta: 37-min dataset, including more patterns. Arrows indicate  $x$  where  $y = 85\%$ .

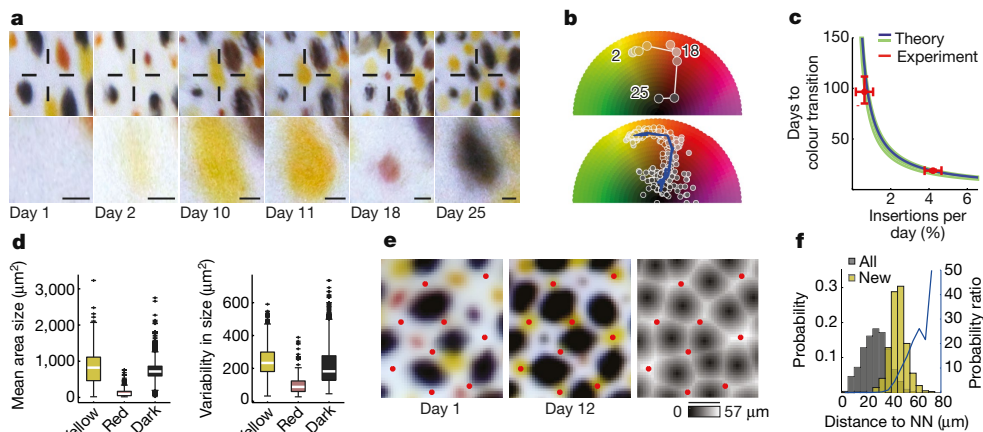


**Fig. 5 | Tracking development of the chromatophore array.** **a**, Aligned images of the same small skin patch over days, illustrating birth and colour changes. Crosshair zoomed-in below. ‘Day 1’ applied post hoc to day preceding detection. Scale bars,  $\sim 50 \mu\text{m}$  (nonlinear alignment). **b**, Top, colour evolution over days for chromatophore in **a**, plotted in hue–value space. Bottom, same for  $n = 13$  chromatophores. After white-balancing, some black chromatophores appear bluish due to noise and are not shown (lower half of the colour wheel). Blue line, median colour over all chromatophores at same estimated developmental time ( $n = 13$ ). **c**, Theoretical relationship between new chromatophore insertion rate and colour maturation (transition to black) for light (L) to dark (D) ratio measured in a juvenile over development (blue), and for the distribution of L/D ratios measured over 1–8-month-old animals (green shows  $\pm 1$  s.d. from the mean,  $n = 7$  animals, see Supplementary Information). Note that experimental measurements (red) fall precisely on the theoretical curve (horizontal error bars: s.e.m., from cross-validation). **d**, Distributions of

We next tested whether the statistical relationships between motor elements might reveal elements of higher-level control<sup>9</sup>. We averaged the time series of all chromatophores in single motor elements to approximate their underlying neural drive (Methods). We then performed hierarchical clustering on the correlation of these average time series, clustering chromatophores that formed motor elements at different levels of granularity.

We illustrate the approach with a dataset in which the animal displayed distinct macroscopic pattern components (Fig. 3e). The first bifurcation (Fig. 3f, top arrow) divided chromatophores within the white square and posterior spots<sup>9</sup> from all the others (Fig. 3g). Within these two superclusters, many degrees of correlation (that is, putative levels of common control) and monochromaticity could be identified. At lower levels in the hierarchy (Fig. 3f, middle arrow), the decomposition revealed medium-sized but still spatially structured elements, such as those that define the borders of the white square (Fig. 3h). Notably, some of these subpattern elements were at times observed to vary independently of their supercluster, consistent with previous brain stimulation experiments, indicating multiple levels of motor control<sup>31</sup> (Supplementary Video 4). In turn, these elements could be decomposed into motor elements (Fig. 3f, bottom arrow), often forming common or collinear patterns indicative of precise innervation, honouring the borders of macroscopic pattern elements (Fig. 3i).

### Tracking pattern dynamics

Changes in the visual scene of an animal usually triggered rapid skin pattern changes. In the example in Fig. 4, a hand was moved above the cuttlefish (Fig. 4a), causing it to transition from dark to light (Fig. 4a and Supplementary Video 5). We examined this transition over several repeats by tracking the states of 17,305 chromatophores at 60 images per second (Fig. 4b–d). Projected into principal component space for visualization, the data took the form of looping trajectories joining dark (Fig. 4b, i) and light (Fig. 4b, ii) states through a sequence of intermediate states (for example, iii; Fig. 4b). Upon each stimulus, the animal not only generated the same target patterns (i and ii) but also moved with

size (left) and standard deviation of size over time (right) for yellow, red (transitional) and dark chromatophores. Transitional chromatophores are significantly smaller and less variable over time than either yellow or dark ones ( $P = 3.5 \times 10^{-92}$  or  $9.7 \times 10^{-107}$ , respectively, Kruskal–Wallis test followed by Tukey’s honest significant difference test;  $n = 1,413$  yellow,  $n = 214$  red,  $n = 1,468$  dark). **e**, New chromatophores arise in gaps in existing array. i, ii, Same skin patch aligned 11 days apart. Red dots centred on chromatophores detected on day 12 but absent on day 1. iii, Greyscale shows distance to nearest older chromatophore in ii. **f**, Summary of insertion location statistics. Dark, distribution of distances to nearest old chromatophore. Yellow, the same distribution, conditioned on location of new chromatophore insertion. Blue line, probability ratio of yellow-to-black distributions, showing an approximately monotonic increase at increasing distances to nearest old chromatophore.  $n = 11,527$  old; 1,412 new chromatophores, 2 animals. NN, nearest neighbour.

chromatophore-level repeatability (Extended Data Fig. 6) through very similar, low-dimensional sequences of intermediate states (Fig. 4c–e: 85% of the variance is explained by nine dimensions). This reliability of sequential chromatophore activation is remarkable because no physical constraints—such as those imposed by a moving limb for example—exist to prevent arbitrary and possibly more direct transitions. This suggests that neural constraints, probably linked to the putative control hierarchy inferred above (Fig. 3 and Extended Data Fig. 7) and to internal connectivity, limit the paths along which pattern transitions can occur.

### Tracking array development

*S. officinalis* continuously add new chromatophores as they grow, increasing from a few thousands in hatchlings to a few millions before death<sup>9</sup>. To track chromatophore insertion and development, we aligned multiple datasets that were recorded days apart (Methods and Supplementary Video 6). We observed that all chromatophores change colour in a systematic progression: all newly born chromatophores were pale yellow (Fig. 5a and Extended Data Fig. 8), consistent with observations in hatchlings<sup>32</sup>. In a seven-day-old animal, yellow chromatophores transitioned over the course of around two weeks to orange and later, briefly, to red. Then,  $18.7 \pm 1.1$  days after detection, each chromatophore turned dark and remained so throughout our observation period, possibly owing to xanthommatin polymerization (Fig. 5b and Extended Data Fig. 8; 13 chromatophores, 25 days). Therefore, the intermediate colours of chromatophores result from at least two causes: their expansion state (Extended Data Fig. 3) and their age (Fig. 5).

Chromatophores (1) do not disappear<sup>33</sup> and (2) their colour ratio (light/dark) is roughly constant ( $1.06 \pm 0.19$  to 1 in seven 8–252-day-old animals)<sup>34</sup>. However, (3) the time over which chromatophores turn from light to dark increased from around 19 days (above) to about 97 days in a 105-day-old animal ( $96.6 \pm 9.3$  days, mean  $\pm$  s.e.m.; Methods). Likewise, whereas light chromatophores are produced daily as a fixed fraction of all existing chromatophores, (4) the rate of chromatophore addition dropped from 4.1% in a seven-day-old animal to

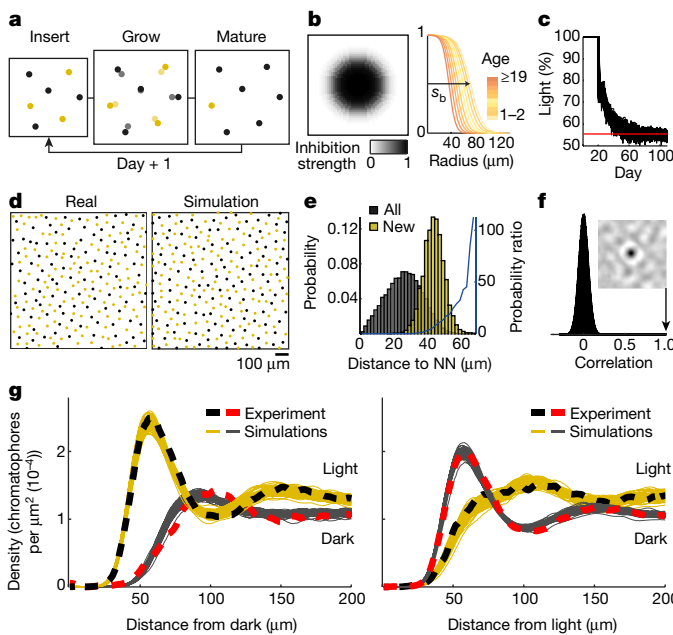


**Fig. 6 | Simple rules explain the spatial layout of chromatophores.** **a**, Schematic of model. Every day, new light chromatophores are inserted into the skin, chromatophores move apart as the skin grows, and chromatophores turn from light to dark when they reach a mature age (19 days). **b**, Left, disc of surround inhibition centred on each chromatophore. Right, radius of inhibitory surround decreases with age at rate  $r_a$  from an initial birth size  $s_b$ . **c**, Percentage of light chromatophores as a function of simulated day (50 runs). Red line, experimental ratio. **d**, Real versus simulated chromatophore position and colour assignment for small skin patches. **e**, Summary of insertion location statistics as in Fig. 5f, but for simulated developing skin. ‘New’ insertions are those on the last ‘day’ of simulation (4 out of 15,494 new insertions at 69–73  $\mu\text{m}$  are not shown for clarity). **f**, Distribution of Pearson’s correlation coefficients between a random patch and all locations of simulated skin. Inset: cross-correlation function centred on the correct matching location, corr. = 1. **g**, Radially averaged density of light and dark chromatophores from the centre of dark (left) and light (right) chromatophores. Dashed lines, experimentally measured densities ( $n = 4,095$  dark; 5,104 light chromatophores). Thin lines, 50 independent runs of the model.

0.6% in a 105-day-old animal. In the Supplementary Information, we provide a formal derivation of an expression linking these observed quantities (2–4). Figure 5c shows the theoretical interdependence of two of these quantities (3 versus 4) given (2): the lifetime of the light state and insertion rate measured experimentally fall precisely on this curve, suggesting that these two properties are balanced to maintain a near-constant colour ratio across the life span of an animal.

The monochromaticity of motor units (Fig. 3a) could result from the fact that new motor neurons<sup>9</sup> innervate only newly born (light) chromatophores<sup>21</sup>. This hypothesis, however, introduces a conundrum in that each animal should keep track of the age of each motor unit to know its colour, an unlikely feat. This problem could be solved, however, if the chromatophores were re-innervated as they change colour, replacing ‘light’ with ‘dark’ motor neurons. Consistent with this, we observed that the average diameter and size variance over time of the red chromatophores were smaller than with the light and dark ones (Fig. 5d and Extended Data Fig. 9), suggesting that motor units undergo re-innervation as they are nearing transition to dark chromatophores.

We next examined the geometry of new-chromatophore insertions. The example in Fig. 5e (i, ii) shows the same aligned patch of skin with an interval of 11 days. The positions of the young (yellow) chromatophores at day 12 (red dots) retrospectively identified the zones of their future insertion as positions far from already born chromatophores (Fig. 5e (iii), 5f). This arrangement suggested a simple model

for the development of the chromatophore array, based on the regulated production of a hypothetical inhibitory signal by each chromatophore<sup>19,35</sup>, which we evaluated using computer simulations.

### Simple rules can explain spatial layout

Our simulation ran on discrete steps (days) and was initiated by the random insertion of light chromatophores in a patch of bare skin, constrained by a chromatophore-centred inhibitory surround (Fig. 6a, b). Once filled with chromatophores, the skin patch ‘grew’ isotropically by a fixed proportion, followed by the next ‘day’ of chromatophore insertion. When chromatophores reached 19 days (above), they switched from light to dark (Fig. 6a). The inhibitory surround was described by a sigmoidal function derived from empirical measurements. To match the experimentally measured differences in spacing between newer and older chromatophores (Fig. 2e and Extended Data Fig. 9), we allowed the size of the inhibitory surround to change as chromatophores age. We fixed the shape of the surround, and fitted its initial size ( $s_b$ ) as well as the rate of size change with age ( $r_a$ ) to empirical measurements (Methods).

Consistent with our analytical results (Fig. 5c), this simple model converged to the observed percentage of light chromatophores (model =  $0.55 \pm 0.01$ , 50 simulations; data = 0.55, 5,104 light/4,095 dark, 1 animal; Fig. 6c), provided the skin growth rate was set to allow a realistic rate of chromatophore insertion (model =  $4.23 \pm 0.01\%$ ; data = 4.1% per day). It produced realistic spatial patterns of light and dark (Fig. 6d), new chromatophore insertion locations (Fig. 6e versus Fig. 5e) and chromatophore density (mean density of chromatophores per  $\mu\text{m}^2$ : model =  $2.52 \times 10^{-4} \pm 0.1 \times 10^{-4}$ ; data =  $2.44 \times 10^{-4}$ ). Local patches of simulated skin had unique spatial layouts (fingerprints) of the type that we exploited for image registration (Fig. 6f versus Fig. 1e). Our model was able to produce realistic local chromatophore-centred densities, featuring the experimentally observed interdigititation of colour-specific modes (Fig. 6g versus Fig. 2e; Extended Data Fig. 9). Notably, by varying  $r_a$ , we could generate other known chromatophore distribution patterns such as the discoid units observed in some squid species<sup>36</sup> (Extended Data Fig. 10). This simple model may thus apply more generally to cephalopod skin patterning.

### Discussion

We developed a strategy to track tens of thousands of individual chromatophores in freely behaving cephalopods, enabling studies of behaviour and development at cellular resolution. Our results open a path towards addressing many important biological questions. A first question concerns visual perception. Cephalopod camouflage is unique in revealing a high-dimensional neural readout of the visual texture perception of an animal. Identifying the primitives of cephalopod camouflage might not only reveal fundamental features of texture generation but also of vertebrate texture perception, because the former (in cephalopods) probably evolved in response to the latter (in their vertebrate predators). A second question concerns the development of methods to analyse very large neural datasets in the context of naturalistic behaviour<sup>37</sup>. Because chromatophore data can be assigned unambiguously to identified elements that lie at the same level of a neural hierarchy (here exclusively motor neurons), their analysis does not suffer from assumptions about their identities and positions in structured or recurrent circuits, as may happen with brain neural imaging. A third question concerns morphogenesis and development. Our data suggest that simple local rules can explain the structure of a continuously growing chromatophore array. They thus lead directly to clear questions about mechanisms and about their similarity with ones known from other systems<sup>38–40</sup>. Fourth, our results indicate that very complex behaviours can be described quantitatively at cellular resolution and in species that may reveal much about shared constraints on brain evolution<sup>41</sup>. This system is therefore particularly well-suited for studying the relationship between neural and behavioural dynamics, a central and general problem in neuroscience.

**Online content**

Any methods, additional references, Nature Research reporting summaries, source data, statements of data availability and associated accession codes are available at <https://doi.org/10.1038/s41586-018-0591-3>.

Received: 31 January 2018; Accepted: 8 August 2018;  
Published online 17 October 18.

1. Messenger, J. B. Cephalopod chromatophores: neurobiology and natural history. *Biol. Rev. Camb. Philos. Soc.* **76**, 473–528 (2001).
2. Beck, J. & Gibson, J. J. The relation of apparent shape to apparent slant in the perception of objects. *J. Exp. Psychol.* **50**, 125–133 (1955).
3. Julesz, B. Visual pattern discrimination. *IRE Trans. Inf. Theory* **8**, 84–92 (1962).
4. Portilla, J. & Simoncelli, E. P. A parametric texture model based on joint statistics of complex wavelet coefficients. *Int. J. Comput. Vis.* **40**, 49–70 (2000).
5. Gatys, L. A., Ecker, A. S. & Bethge, M. A neural algorithm of artistic style. Preprint at <https://arxiv.org/abs/1508.06576v2> (2015).
6. Ghiasi, G., Lee, H., Kudlur, M., Dumoulin, V. & Shlens, J. Exploring the structure of a real-time, arbitrary neural artistic stylization network. Preprint at <https://arxiv.org/abs/1705.06830v2> (2017).
7. Cloney, R. A. & Florey, E. Ultrastructure of cephalopod chromatophore organs. *Z. Zellforsch. Mikrosk. Anat.* **89**, 250–280 (1968).
8. Florey, E. & Kriebel, M. E. Electrical and mechanical responses of chromatophore muscle fibers of the squid, *Loligo opalescens*, to nerve stimulation and drugs. *Z. Vergl. Physiol.* **65**, 98–130 (1969).
9. Hanlon, R. T. & Messenger, J. B. Adaptive coloration in young cuttlefish (*Sepia officinalis* L.): the morphology and development of body patterns and their relation to behaviour. *Phil. Trans. R. Soc. B* **320**, 437–487 (1988).
10. Kelman, E. J., Osorio, D. & Baddeley, R. J. A review of cuttlefish camouflage and object recognition and evidence for depth perception. *J. Exp. Biol.* **211**, 1757–1763 (2008).
11. Gonzalez-Bellido, P. T., Scaros, A. T., Hanlon, R. T. & Wardill, T. J. Neural control of dynamic 3-dimensional skin papillae for cuttlefish camouflage. *iScience* **1**, 24–34 (2018).
12. Dubas, F., Hanlon, R. T., Ferguson, G. P. & Pinsker, H. M. Localization and stimulation of chromatophore motoneurones in the brain of the squid, *Lolliguncula brevis*. *J. Exp. Biol.* **121**, 1–25 (1986).
13. Florey, E., Dubas, F. & Hanlon, R. T. Evidence for L-glutamate as a transmitter substance of motoneurons innervating squid chromatophore muscles. *Comp. Biochem. Physiol. C* **82**, 259–268 (1985).
14. Reed, C. M. The ultrastructure and innervation of muscles controlling chromatophore expansion in the squid, *Loligo vulgaris*. *Cell Tissue Res.* **282**, 503–512 (1995).
15. Liddell, E. G. T. & Sherrington, C. S. Recruitment and some other features of reflex inhibition. *Proc. R. Soc. Lond. B* **97**, 488–518 (1925).
16. Ho, T. K. Random decision forests. In *Proc. 3rd International Conference on Document Analysis and Recognition* 278–282 (IEEE Computer Society, 1995).
17. Lucas, B. D. & Kanade, T. An iterative image registration technique with an application to stereo vision. In *Proc. 7th International Joint Conference on Artificial Intelligence* 674–679 (Morgan Kaufmann, 1981).
18. Mäthger, L. M., Chiao, C. C., Barbosa, A. & Hanlon, R. T. Color matching on natural substrates in cuttlefish, *Sepia officinalis*. *J. Comp. Physiol. A* **194**, 577–585 (2008).
19. Bassaglia, Y. et al. *Sepia officinalis*: a new biological model for eco-evo-devo studies. *J. Exp. Mar. Biol. Ecol.* **447**, 4–13 (2013).
20. Fioroni, P. Die embryonale Genese der Chromatophoren bei *Octopus vulgaris* Lam. *Acta Anat.* **75**, 199–224 (1970).
21. Packard, A. Morphogenesis of chromatophore patterns in cephalopods: are morphological and physiological ‘units’ the same? *Malacologia* **23**, 193–201 (1982).
22. Deravi, L. F. et al. The structure–function relationships of a natural nanoscale photonic device in cuttlefish chromatophores. *J. R. Soc. Interface* **11**, 20130942 (2014).
23. Dubas, F. Innervation of chromatophore muscle fibers in the octopus *Eledone cirrhosa*. *Cell Tissue Res.* **248**, 675–682 (1987).
24. Ferguson, G. P., Martini, F. M. & Pinsker, H. M. Chromatophore motor fields in the squid, *Lolliguncula brevis*. *J. Exp. Biol.* **134**, 281–295 (1988).
25. Messenger, J., Cornwell, C. & Reed, C. L-glutamate and serotonin are endogenous in squid chromatophore nerves. *J. Exp. Biol.* **200**, 3043–3054 (1997).
26. Maynard, D. M. in *Invertebrate Nervous Systems: Their Significance for Mammalian Neurophysiology* (ed. Wiersma, C. A. G.) 231–255 (Univ. Chicago Press, Chicago, 1967).
27. Dubas, F. & Boyle, P. R. Chromatophore motor units in *Eledone cirrhosa* (Cephalopoda: Octopoda). *J. Exp. Biol.* **117**, 415–431 (1985).
28. Florey, E. Nervous control and spontaneous activity of the chromatophores of a cephalopod, *Loligo opalescens*. *Comp. Biochem. Physiol.* **18**, 305–324 (1966).
29. Bell, A. J. & Sejnowski, T. J. An information-maximization approach to blind separation and blind deconvolution. *Neural Comput.* **7**, 1129–1159 (1995).
30. Hyvärinen, A. & Oja, E. Independent component analysis: algorithms and applications. *Neural Netw.* **13**, 411–430 (2000).
31. Boycott, B. B. The functional organization of the brain of the cuttlefish *Sepia officinalis*. *Proc. R. Soc. Lond. B* **153**, 503–534 (1961).
32. Andouche, A. & Bassaglia, Y. Coleoid cephalopod color patterns: adult skin structures and their emergence during development in *Sepia officinalis*. *Vie Milieu* **66**, 43–55 (2016).
33. Packard, A. Size and distribution of chromatophores during post-embryonic development in cephalopods. *Vie Milieu* **35**, 285–298 (1985).
34. Yacob, J. et al. Principles underlying chromatophore addition during maturation in the European cuttlefish, *Sepia officinalis*. *J. Exp. Biol.* **214**, 3423–3432 (2011).
35. Packard, A. & Hochberg, F. G. Skin patterning in *Octopus* and other genera. *Symp. Zool. Soc. Lond.* **38**, 191–231 (1977).
36. Hanlon, R. T. The functional organization of chromatophores and iridescent cells in the body patterning of *Loligo plei* (Cephalopoda: Myopsida). *Malacologia* **23**, 89–119 (1982).
37. Gomez-Marin, A., Paton, J. J., Kampff, A. R., Costa, R. M. & Mainen, Z. F. Big behavioral data: psychology, ethology and the foundations of neuroscience. *Nat. Neurosci.* **17**, 1455–1462 (2014).
38. Yamaguchi, M., Yoshimoto, E. & Kondo, S. Pattern regulation in the stripe of zebrafish suggests an underlying dynamic and autonomous mechanism. *Proc. Natl Acad. Sci. USA* **104**, 4790–4793 (2007).
39. Cheng, C. W. et al. Predicting the spatiotemporal dynamics of hair follicle patterns in the developing mouse. *Proc. Natl Acad. Sci. USA* **111**, 2596–2601 (2014).
40. Manukyan, L., Montandon, S. A., Fofonka, A., Smirnov, S. & Milinkovitch, M. C. A living mesoscopic cellular automaton made of skin scales. *Nature* **544**, 173–179 (2017).
41. Kröger, B., Vinther, J. & Fuchs, D. Cephalopod origin and evolution: a congruent picture emerging from fossils, development and molecules: extant cephalopods are younger than previously realised and were under major selection to become agile, shell-less predators. *BioEssays* **33**, 602–613 (2011).

**Acknowledgements** We thank F. Bayer, A. Umminger and N. Heller for assistance in building the experimental setup; L. Jürgens, T. Klappich, J. Nenninger, E. Northrup and G. Wexel for animal care; R. Siegel for providing the squid skin image; E. Lamo Peitz, S. Trägenap and J. Racky for help with image alignment and segmentation; R. Hanlon and members of the Marine Biology Laboratory in Woods Hole for their hospitality to G.L. in the summer of 2016; Bruker Daltonics, J. Fuchser and C. Henkel for Fourier-transform ion cyclotron resonance–mass spectrometry measurement time and discussions; M. Tosches and L. Fenk for comments on the manuscript; and the members of the Laurent laboratory for discussions. Funded by the Max Planck Society (G.L.), the European Research Council (G.L.) and the Bernstein Focus: Neurotechnology Frankfurt (M.K.).

**Reviewer information** *Nature* thanks C. Machens, D. Osorio and the other anonymous reviewer(s) for their contribution to the peer review of this work.

**Author contributions** G.L. conceived, initiated and managed the project. S.R., T.W., M.A.L., J.S.E., L.A.A., A.L. and G.L. designed and conducted the experiments. P.H., S.R., F.K. and M.K. developed and implemented the image-processing pipeline. J.M.-C. and J.D.L. carried out the mass-spectrometry analysis. M.A.L. developed the analytical model of colour evolution with input from M.K. S.R. developed and ran the numerical simulations with input from M.K. S.R., P.H., M.A.L., T.W., J.S.E., M.K. and G.L. analysed and discussed all data. G.L. and S.R. wrote the text with input from all authors.

**Competing interests** The authors declare no competing interests.

**Additional information**

**Extended data** is available for this paper at <https://doi.org/10.1038/s41586-018-0591-3>.

**Supplementary information** is available for this paper at <https://doi.org/10.1038/s41586-018-0591-3>.

**Reprints and permissions information** is available at <http://www.nature.com/reprints>.

**Correspondence and requests for materials** should be addressed to G.L.

**Publisher's note:** Springer Nature remains neutral with regard to jurisdictional claims in published maps and institutional affiliations.

## METHODS

**Experimental animals.** Animal experimentation in this study was performed according to German animal welfare law (paragraph 11, sentence 1, #1, German animal welfare law to house and breed cephalopods for scientific purposes). European cuttlefish *S. officinalis* were hatched from eggs collected in the English Channel and reared in a seawater system, at 20 °C. The closed system contains 4,000 l of artificial seawater (ASW; Instant Ocean) with a salinity of 33‰ and pH of 8–8.5. Water quality was tested weekly and adjusted as necessary. Trace elements and amino acids were supplied weekly. Marine LED lights above each tank provided a 12/12-h light/dark cycle with gradual on- and off-sets at 07:00 and 19:00. The animals were fed live food (either *Hemimysis* spp. or small *Palaemonetes* spp.) ad libitum three times per day. Experimental animals of unknown sex were selected for healthy appearance and calm behaviour. The animals were housed together in 120-l glass tanks with a constant water through-flow resulting in five complete water exchanges per hour. Enrichment consisted of natural fine-grained sand substrate and seaweed (*Caulerpa prolifera*).

**In vivo behavioural data acquisition.** For in vivo behavioural experiments, six animals (1 to 60 days post-hatching, around 6–50 mm in mantle length) were placed in a capped filming chamber (150 mm × 95 mm × 75 mm or 240 mm × 170 mm × 50 mm) filled with seawater. A single filming session typically lasted between 10 and 90 min per day and per animal. Our filming procedures induced no pain, suffering, distress or harm to the animal. Naturalistic textures with normalized power spectra (Normalized Brodatz Texture database) and artificial patterns generated in MATLAB and Paint were displayed on the floor of the tank using an E-Ink display. Filming was performed at 59.94 frames per second (f.p.s.) in 4K full-frame (4,096 × 2,160) using the Sony PMW-F55 camera in the Sony RAW format. Resolution was  $40.8 \pm 32.4 \mu\text{m}^2$  per pixel. The camera was mounted on a motorized x-y translation stage and its position adjusted with a joystick to keep the animal in view. Acquired data were colour matched in DaVinci Resolve Studio 12.5 (Black Magic Design). Movies were compressed offline to the H.264 format using the x264 encoder provided by FFmpeg-2.8.6, with the compression preset ‘faster’ and the constant rate factor of 16, without chroma subsampling. These compressed movies were used for all subsequent in vivo data analysis. Note that the analyses and results presented in this paper do not depend on the exact statistics of the images or patterns shown to the animals. They depend only on our ability to detect changes and correlations between patterns produced by single animals over time, at sub-chromatophore resolution.

**In vitro electrophysiology.** For in vitro experiments, animals (19–40 weeks old,  $115 \pm 28$  mm in mantle length, 10 in total) were euthanized according to well-established best-practice protocols<sup>42</sup>: animals were deeply anaesthetized first in isotonic 3% ethanol in ASW and then in 5% ethanol in ASW or using 3.5% (w/v) MgCl<sub>2</sub> in ASW. Superficial skin samples were then removed gently from the dorsal mantle, peeling away the superficial skin layers from the underlying body musculature, gently cutting nerves and connective tissue with iridectomy scissors and taking care that the chromatophores were not overly stretched or damaged. These skin samples were placed in cold ASW inside a transparent observation chamber, pinned at their edges, superficial surface down, stretched gently so as to eliminate wrinkles and left to recover. The chamber was placed on the translation stage of an inverted microscope and the chromatophore array observed with 1.25 × or 2.5 × objectives (126.75 or 291.78 pixels per mm). A fine suction electrode operated with a micromanipulator was placed on the cut end of a nerve and for electrical stimulation (pulse duration: 100 µs) at pulse rates of 0.5 Hz and at threshold intensity using a pulse generator (from  $\pm 5.57$  to  $\pm 2,774 \mu\text{A}$  dialled up gradually, A.M.P.I., Master-8-cp) and a constant-current stimulus isolator (World Precision Instruments, A360). Colour images of the chromatophores were acquired with a CCD/CMOS camera (Basler acA1920-155uc) at 30 f.p.s. The stimulus trace and camera exposure times were recorded using a digitizer (Axon Digidata 1440A). Synchronization and analysis were conducted offline.

**Transmission spectra.** Transmission spectra were recorded from fresh skin samples (extracted as above). Samples were mounted on standard microscope slides with #1.5 coverslips in ASW. Transmission spectra were recorded in 32 channels on a Zeiss LSM 880 Examiner confocal microscope (10×, NA 0.45, water immersion objective) using the ‘lambda mode’ spectral detection. This mode is usually intended for fluorescence detection, but the halogen lamp for transmitted-light mode can be turned on with a service macro. Images were thus recorded with a scanned point detector but with wide field illumination. We manually drew regions of interest around chromatophores. Raw spectra were normalized with respect to a nearby region in the same field of view that did not contain any chromatophores. To measure the effect of expansion state on transmission spectra, ASW was replaced by a glutamate solution (40 µM) in ASW. Images were acquired before and 6–8 min after glutamate application.

**Mass spectrometry.** Excised skin tissue samples were homogenized in 1:1 methanol:water (v/v) supplemented with 1% trifluoroacetic acid, sonicated for 10 min in an ultrasonic bath and placed for 2 h on a rotary shaker. The samples

were then centrifuged for 10 min, the supernatant removed, filtered through a 0.2-µm syringe filter and evaporated to dryness. For mass spectrometry, the dried extracts were resuspended in 95:5 water:acetonitrile (v/v) supplemented with 0.1% formic acid.

High-performance liquid chromatography coupled to ultraviolet light (UV) absorption and mass spectrometric detection (HPLC–UV–MS) experiments were carried out on an Ultimate 3000 RSLC system (Dionex) equipped with a CSH C18 column (Charged Surface Hybrid, 2.1 × 100 mm, 1.7-µm particle size, Waters) and variable wavelength detector set to 250 nm, coupled to an Impact II mass spectrometer (Bruker Daltonik). Separation was carried out using water (A) and acetonitrile (B), both supplemented with 0.1% formic acid, as mobile phases with a flow rate of 300 µl min<sup>-1</sup> at 40 °C. After 2 min of equilibration with 2% B, a linear gradient was ramped from 2% to 95% B in 30 min followed by 5-min wash (95% B) and 3-min equilibration (2% B) steps. The mass spectrometer was operated in positive-ion mode with a mass range of *m/z* 50–1,000. Processing and data analysis were performed manually using DataAnalysis 4.4 (build 200.55.2969, Bruker Daltonik).

For direct infusion experiments, extracts were diluted 1:100 and infused at 120 µl h<sup>-1</sup> into a 7T SolariX XR mass spectrometer (Bruker Daltonik). Spectra were recorded in positive-ion mode of *m/z* 107.5–2,000. For exact mass determination and fragmentation experiments, precursor ions were isolated using the quadrupole, inspected for contaminating ions and then subjected to collision-induced dissociation in the collision cell. Spectra were analysed with DataAnalysis 4.4 (build 200.55.2969, Bruker Daltonik).

For mass spectrometry imaging experiments, excised skin tissue samples were stretched and pinned onto frozen gelatine blocks, snap-frozen in isopentane and sectioned to 12 µm using a CM 3050s cryotome (Leica Biosystems). The slices were carefully transferred onto conductive ITO-coated glass slides (Bruker Daltonik), thaw-mounted and dried in a vacuum desiccator before taking optical slide scans with an OpticLab H850 histology slide scanner (Plustek). Samples were screened using a Rapiflex TOF/TOF mass spectrometer (Bruker Daltonik) operated in positive- and negative-ion modes, using a mass range of *m/z* 100–2,000. Ultrahigh-resolution mass spectra were acquired on a 7T SolariX XR mass spectrometer (Bruker Daltonik) in positive-ion mode in a mass range of *m/z* 107.5–2,000 using a 20 µm × 20 µm pixel grid. The laser was operated at 500 Hz with 100 shots per pixel and focus set to minimum. Imaging data were acquired and pre-processed using flexImaging 5.0 (build 5.0.78.0\_1031\_152, Bruker Daltonik) and further analysed and visualized using SCiLS Lab 2016b (build 4.01.8758, SCiLS). Individual images were adjusted to the same intensity scale and weak spatial denoising was applied for merged compounds. Spatial segmentation was performed with weak spatial denoising and a bisecting k-means algorithm based on the correlation distance of individual spectra. The relationship between colour and xanthommatin concentration was examined by manually clustering partitions of the k-means algorithm, corresponding to yellow and red-brown chromatophores.

**Summary of the image processing and tracking pipeline.** The major steps of the processing pipeline were as follows: (1) chunking: identify episodes of video ('chunks') with cuttlefish in focus; (2) segmentation: label pixels as chromatophore or background on individual frames; (3) registration: alignment across frames within chunks to correct nonlinear body distortions (over seconds); (4) stitching: alignment across chunks (seconds to hours); (5) chromatophore identification and size tracking; (6) colour assignment; and (7) stitching across days.

**Chunking of in-focus frames.** In vivo behavioural datasets consisted of series of frames in which the animal was in view and in focus, separated by frames in which the animal was out of view, out of focus or blurred owing to fast motion. We first identified in-focus frames using a simple focus statistic (sum of a difference-of-Gaussians filter size 15 × 15 pixels,  $\sigma = 1.5$  and 2 pixels) to each image. The standard deviation of the filter was selected to match the mean size of chromatophores. Our statistics therefore indicated whether chromatophores were present and clear in an image. Continuous sequences of images were then selected semi-automatically, based on the amplitude of the focus statistic and its variability over images and time. We called continuous in-focus image sequences obtained within a single filming session ‘chunks’.

**Chromatophore segmentation.** We segmented chromatophores from the background using a supervised learning approach. For training and validation, images (1 each) of 256 × 256 pixels containing a representative sampling of chromatophore sizes and colours were manually annotated pixel-wise as belonging to a chromatophore or background skin. Annotations were performed by six individuals and inconsistencies were removed using majority vote. We then fitted a random-forest model<sup>16</sup> to this annotation. Our model classified pixels as chromatophore or background based on feature vectors calculated from the output of eight difference-of-Gaussian filters ( $\sigma = 0.8^{1.4x}$ ,  $x = 1:8$ ) per RGB colour channel. Filter sizes were chosen to cover the range of observed chromatophore sizes. We determined the random forest parameters by hyperparameter optimization<sup>43</sup> (number of trees in 1–32, maximal depth in 1–32, minimal data size for split in 1–11, minimal data size for leaves 1–21, splitting criterion either by Gini impurity or information gain and

enabling or disabling bootstrap aggregation). Then, 1,000 models were fitted using a fourfold cross-validation and the best model was identified by the  $F_1$  score. To this end, we used a model with eight trees with a depth of 8 and an entropy-based splitting criterion on five randomly selected features. We assessed model performance by comparing classifier performance against a second, manually annotated image (Extended Data Fig. 1).

**Alignment of images within a chunk.** Animal movement (for example, breathing) and skin distortions caused the pixel location of chromatophores to change over frames. Our high frame rate combined with the definition of chunking meant that differences in chromatophore locations (both affine and non-affine deformations) between successive frames within a chunk could be assumed to be small. We could therefore use image registration methods for small-displacement optic flow. We used the Lukas–Kanade optical flow algorithm<sup>17</sup> to track points centred on a random subset of around 300 round chromatophores. Round chromatophores were found by placing a threshold on circularity of chromatophores detected in the first frame of the chunk. These chromatophores were selected to minimize runtime. The full-frame optical flow was interpolated from these tracking points using a moving least-squares algorithm<sup>44</sup>. We chose a smoothness parameter ( $\alpha = 3$ ) for interpolation to remove skin distortions and large movement, but not the fine scale movement of individual chromatophores.

**Stitching averaged aligned images over chunks.** Once all the images within a chunk were aligned, we averaged over the binarized images, generating a ‘master frame’. The value of each pixel in a master frame thus represents the fraction of frames within the corresponding chunk in which that pixel was labelled as belonging to a chromatophore. Because chromatophore size can vary over frames during a single chunk, the typical profile of a chromatophore in a master frame is a radial gradient. After obtaining one master frame per chunk, we developed a method to register all of the chunks of a filming session into a common reference frame. We call this process ‘stitching’. Individual chunks were, by definition, separated from each other by out-of-focus epochs, that is, frames in which the cuttlefish often changed position, angles in  $x$ ,  $y$  and  $z$ , body shape and chromatophore pattern. Stitching thus required aligning and morphing chunks into the same reference frame. For every master frame in a dataset, we first defined a mask outlining the cuttlefish by applying a difference-of-Gaussian filter to the image and thresholding the result. We then mapped all master frames into each other’s reference frames.

To stitch together two master frames ‘A’ and ‘B’, we first performed a coarse rigid-body transform mapping A into the reference frame of B by fitting an ellipse around the cuttlefish mask in both frames. This created B’, that is, B mapped into the reference frame of A through the inverse of this mapping. Next, we defined a grid of points  $256 \times 256$  pixels apart over the cuttlefish mask of A. We attempted to find each point of this grid in B’ by correlating patches of  $64 \times 64$  pixels centred on the grid points in A with regions in B’. We sampled a range of translations ( $\pm 256$  pixels in 2-pixel steps) and rotations ( $\pm 20^\circ$  in  $2^\circ$  steps) around the pixel location of each grid point to find the pixel with the highest correlation value. In general, not all of the grid points could be correctly mapped; outliers were removed using the RANSAC algorithm<sup>45</sup> under an affine model. A new map was constructed from the remaining mapped points using moving least squares interpolation<sup>44</sup>.

By applying the inverse of this mapping to B’ we produced B”, a more refined mapping. Fine alignment was performed by repeating this process on a finer grid. A new grid of points  $32 \times 32$  pixels was defined on the cuttlefish mask of A. We then attempted to find each of the points in B” with the highest local cross-correlation to  $64 \times 64$ -pixel patches centred on each grid point. We then interpolated between these points using moving least squares to produce a full map, B”. Combining these three maps resulted in a single non-affine mapping from B into the reference frame of A.

This stitching algorithm was used to map every master frame in a dataset into the reference frame of every other master frame. We could quantify the accuracy of this non-symmetric mapping over the cuttlefish mantle by calculating the reprojection error: all points in the cuttlefish mask of master frame A were mapped into the reference frame of master frame B (using the A-to-B map) and then mapped back into the reference frame of A (using the B-to-A map). The reprojection error was defined as the Euclidian distance between the original and remapped points. A point was considered well-mapped if it reprojected to within three pixels ( $20 \pm 6 \mu\text{m}$ ) of its original location. By taking the fraction of well-mapped points in every master frame, we produced a matrix quantifying how well every master frame mapped into every master frame over the cuttlefish mantle. The column of this matrix with the highest well-mapped fraction identified the master frame into which all others mapped best. We used this as common reference frame for the dataset (see ‘Chromatophore definition’). Poorly mapped chunks of data, defined as master frames that had less than 50% well-mapped points within the cuttlefish mask were excluded from subsequent analysis. Stitching failures were usually the result of poorly registered chunks, resulting in blurry master frames. These failures,

in turn, were often due to temporary loss of focus through cuttlefish moving in and out of the focus range of our optical system.

**Chromatophore definition.** As done for within-chunk alignment, we used the maps generated by our stitching algorithm to project all master frames into the common reference frame of each dataset. The resulting average frame (the ‘queen frame’) represented approximately the probability of each pixel being labelled as belonging to a chromatophore throughout all in-focus frames over the entire filming session, excluding poorly mapped chunks of data (see ‘Stitching averaged aligned images over chunks’). Chromatophores were detected by finding local maxima using a  $3 \times 3$  footprint kernel. Applying the watershed transform to the queen frame with detected chromatophores as markers divided the image into basins, each defining a region surrounding a single chromatophore. The watershed transform also split groups of merged chromatophores, relying on gradients in the queen frame created by chromatophore size changes over the dataset. A conservative mask defining the region of the cuttlefish mantle that was in focus was drawn as a convex hull of manually selected points, and all subsequent analysis was performed on chromatophore basins within this masked region.

**Chromatophore-size tracking.** With the chromatophore basins so defined, we could track the expansion state of each chromatophore over time. Each segmented image (see ‘Chromatophore segmentation’) was mapped into the reference frame of the first image in a chunk (see ‘Alignment of images within a chunk’), and then mapped again into the common reference frame of the dataset (see ‘Stitching average aligned images over chunks’). The number of pixels classified as belonging to chromatophores in the segmented image was counted in every watershed basin of the queen frame. This pixel number, multiplied by an experiment-specific  $\mu\text{m}$  per pixel calibration, defined the area of each chromatophore in each frame. This calculation was repeated with all images in a dataset, producing parallel time-series measurements of size over time for all segmented chromatophores. Although chromatophore size generally varies with mantle position as the animal adopts different skin patterns, a uniformly dark pattern, as seen in Fig. 4a, reveals no strong correlation between chromatophore size and either anterior–posterior or medial–lateral position ( $r = 0.06$  or  $r = -0.03$ , respectively).

**Colour assignment.** Determining the colour of chromatophores is difficult to accomplish accurately on single images *in vivo* owing to camera pixel noise, variability in lighting and the expansion-state dependency of chromatophore colour. We therefore analysed chromatophore colours by mapping all images of a dataset into the common reference frame of the dataset, producing an average colour image. We first constructed a feature space in which chromatophores could be accurately colour-labelled independently of our segmentation algorithm. We high-pass filtered the image and then performed independent component analysis in colour space<sup>29,30</sup>. After projecting the image onto the two largest independent components and thresholding each projection separately, we took the maximum value over projections. This image was smoothed with a Gaussian filter (s.d. = 1 pixel). We then applied a watershed algorithm<sup>46</sup> to identify chromatophore regions. Chromatophore centres were defined as the weighted centroid of each region. Visible chromatophores that were not detected automatically, typically smaller red and yellow chromatophores, were identified manually. The average RGB value of a region of  $3 \times 3$  pixels of the average colour image, centred on the location of each chromatophore, defined chromatophore colour. These colours were clustered into two classes by fitting a Gaussian mixture model. We observed no strong correlation between the anterior–posterior or medial–lateral position on the mantle and chromatophore colour label ( $r = -0.0047$  or  $r = -0.0029$ ). We defined the colour of tracked chromatophores by performing a nearest-neighbour matching between chromatophore centres defined using our tracking pipeline and centres defined on the average colour image. For the motor element inference experiments, 93% of dark and 82% of light chromatophores that were detected in the average colour image ( $n = 39,948$ ) could be linked to a tracked chromatophore ( $n = 35,062$ ) located within three pixels ( $15.1 \pm 5.9 \mu\text{m}$ , from three animals).

**Stitching over filming sessions and detecting new chromatophores.** We filmed two additional animals over periods of several weeks, that is, periods over which the animals underwent considerable growth. To track chromatophores over days and weeks, we used a modified version of our stitching algorithm (see ‘Stitching average aligned images over chunks’). To model cuttlefish growth, we used a similarity transformation rather than a rigid-body transformation in the initial coarse alignment of cuttlefish masks. In the subsequent two correlation-matching steps, we use a larger search space in scales, rotations and translations. We used the resulting map to warp the queen frame of one dataset into the reference frame of another dataset. After this, we linked chromatophores over days through a nearest-neighbour matching. A convex hull containing the intersection of the chromatophore basins from both datasets was first calculated, and matching was only performed within this region. New chromatophores were defined as chromatophores from the later dataset that were located within the convex hull intersection and were not matched with a chromatophore in the earlier dataset. In total,  $75 \pm 14\%$  of the pixels in the convex hull that contained mapped

chromatophores had reprojection errors below 50 µm (six datasets mapped from three animals), allowing for unambiguous matching through manual inspection and modification of matches using a custom graphical user interface.

**Pipeline implementation.** Our alignment and tracking pipeline was implemented on two computing clusters: the Draco supercomputer at the Max Planck Computing and Data Facility, where 16 jobs were processed in parallel on 1–2 nodes with 32 cores at 2.3 GHz (128 Gb RAM per node); and the FIAS computing cluster, where 3 jobs were processed in parallel on 2–4 nodes with 32–64 cores per node at 2.6 GHz (64 Gb RAM per node). Data management between local storage and compute nodes was managed by a Bash script determining the sending and receiving of data and configuration files, and starting the pipeline on compute nodes. On each compute node, the pipeline computations were managed by a second Bash script, which inserted all pipeline steps into a SLURM<sup>47</sup> queue. Parallel computation of the steps was handled by the SLURM controller. Parallelization per step was achieved by spawning programs using MPI<sup>48</sup>, and distributing computations across program instances. For steps for which random access across video frames could not be implemented (for example, reading a video), MPI spawned programs following a one-producer/multiple-consumers pattern. For registration, parallelization was achieved by distributing the optical flow and moving least-squares algorithms across program instances. Threading was done using third-party libraries. The pipeline was written for GNU/Linux operating systems in the Python and Cython programming language, relying on Scipy<sup>49</sup>, scikit-learn<sup>50</sup>, scikit-image<sup>51</sup>, PyQt and OpenCV-Python. Further data analysis was performed in Python and MATLAB. The results of all pipeline steps were stored using the HDF5 format. The pipeline was constructed so that each step read one file and output another. In total, we achieved an overall speed of around 1–1.5 frames s<sup>-1</sup> (corresponding to around 2.4–3.6 Mb s<sup>-1</sup> of a compressed video).

**Chromatophore-triggered density plots.** We constructed images composed of the locations of certain chromatophores (light, dark and so on) and then averaged regions of these images centred on the location of chromatophore classes of interest. The resulting chromatophore-triggered average image was linearly interpolated to 1 pixel per µm<sup>2</sup> and then smoothed with a Gaussian filter (15 µm size, 2–3 µm s.d.) We then computed radial averages.

**Automated extraction of motor units (in vitro experiments).** Consecutive frames were first aligned using optic flow (see ‘Alignment of images within a chunk’) to correct for spontaneous skin movements. For experiments containing >7 consecutive stimulus trials, the nearest video frames between 10-ms pre- and 200-ms post-stimulus were inspected and annotated manually for expansion events using image subtraction. Chromatophore position and colour were determined from the pre-stimulus frame of the first expanding trial. Colour classification was made using a threshold on the red channel of the white-balanced, contrast-stretched RGB space. Motor units were identified by coincident responses and failures of a set of multiple chromatophores (>1) across trials, allowing for an individual failure rate of up to 25%. We estimated the average spontaneous expansion probability (of 0.0293) by examining the activity of 81 chromatophores from four animals at times without stimulation. We then could estimate the chance probability of an observed sequence of responses and failures as

$$\binom{n}{e} (r^m)^e ((1-r)^m)^{n-e}$$

in which  $m$  is the number of chromatophores in a putative motor unit,  $e$  is the number of expansion trials and  $n$  is the total number of trials. A threshold of  $P = 0.05$  was placed on observed sequences for inclusion as a motor unit. Motor units along the edge (mean + 1 s.d. of the average chromatophore nearest-neighbour distance) of the field of view were excluded from the analysis to prevent underestimation of motor unit size.

**Inference of motor elements from in vivo imaging data.** Our choice of statistical model for motor unit inference was motivated by the desire to capture the potentially overlapping innervation of motor units while excluding sets of chromatophores that are more transiently coordinated.

Chromatophore-area time series were symmetrically low-pass filtered to 4 Hz using a 3-pole Butterworth filter. They were then downsampled 4–8-fold. We performed a ‘spatial’ ICA on the resulting matrix, using the Fast ICA algorithm<sup>30</sup>. This algorithm iteratively estimates  $S = WX$ , in which  $X$  is the centred, whitened, area-traces  $\times$  chromatophore matrix,  $W$  is the unmixing matrix, and  $S$  is the component  $\times$  chromatophore matrix of independent components. We used the algorithm to estimate  $C$  independent components, in which  $C$  is the number of dimensions explaining 99.5% of the variance of a dataset.

To estimate statistically small sets of chromatophores receiving common drive (‘motor elements’, see main text), we subsequently clustered the small subset of chromatophores with high values on single independent components of the matrix  $S$ . Because motor-unit membership is binary (a chromatophore either is innervated by a motor neuron or is not), we thresholded the independent components to extract these highly contributing chromatophores and examine their properties.

We found that the highest contributing chromatophores most often clustered spatially in single modes, with chromatophores contributing less located further away. We chose our threshold for motor-element inclusion such that the median of the chromatophore spatial distribution matched approximately that measured in vitro. We assigned a sign to each independent component as the sign of the maximum value (chromatophore) of that independent component. Values higher than 8 s.d. above the mean value of the positive independent components or lower than 8 s.d. below the mean value of the negative independent components were clustered to form a motor element. We then visually inspected the motor elements to check for colour classification errors and to remove groups that did not contain well-segmented chromatophores due to errors in watershedding.

**Inference of putative motor control hierarchy.** We first averaged the filtered, downsampled area time series (as in ‘Inference of motor elements from in vivo imaging data’) for all chromatophores assigned to a motor element (ignoring the sign or weight of its associated independent component). This procedure was motivated by the known underlying biology: it attempted to approximate the common motor neuron drive that caused the chromatophores to be clustered into a motor element. Note that the precision of this approximation depends on several factors, including the multiple and partially overlapping innervation of chromatophores, the difficulties of inferring motor units (as described above) and the fact that the relationship between chromatophore size and neural drive is likely to be sigmoid, and thus linear only in a limited range. We performed agglomerative hierarchical clustering of these time series of motor elements, using the correlation coefficient as a distance metric and complete linkage. To segment monochromatic clusters at different levels of the hierarchy, we measured the fraction of clusters composed of motor elements that contained only light or only dark chromatophores.

**Chromatophore colour changes over development.** For precise characterization of chromatophore colours (Fig. 5a, b), we took images of two cuttlefish over days using an 18-M-pixel camera (Canon, 550D) at 10–18× magnification. Recognizable landmarks (for example, papillae and mantle edges) were used to return to the same area of skin repeatedly. We aligned skin patches using TrakEM2 (ImageJ plugin). Images of chromatophores were white-balanced using a nearby patch of skin that did not contain any chromatophore as a reference. The colour of individual chromatophores was then determined in hand-drawn regions of interest (ROIs). To visualize the colour change in a condensed representation in colour space, the three colour channels (red, green and blue) were averaged over all pixels within the ROI. Colours were then converted from RGB into hue-saturation-value colour space, which assigns brightness and hue to different axes. To determine an average trajectory in colour space, the chromatophores were temporally aligned to the transition state by thresholding on the red colour channel.

**Chromatophore sizes over development.** To check for potential size and variability differences of the transition state, we aligned a dataset separated by two days using our pipeline and identified transitioning chromatophores as those that were classified as light on the earlier day and dark on the later one. Yellow chromatophores were defined as light chromatophores that were not transitioning. Size and variability were estimated using filtered data (as in ‘Inference of motor elements from in vivo imaging data’). For validation independent of our tracking pipeline (Extended Data Fig. 9c), we aligned images using TrakEM2, and manually grouped individual chromatophores into three categories (yellow/orange, reddish-brown, black) without temporal context. We then incorporated developmental information by retaining only those yellow/orange chromatophores that were observed again at a later time point as yellow/orange, that is, those data, that were not close to the transition. Similarly, black chromatophores were retained only if they were observed earlier already as black. Size was determined on hand-drawn ROIs outlining each chromatophore in the aligned dataset.

**Colour-development-numbers model.** For the juvenile animal, the generation rate of new chromatophores was estimated by counting, in datasets aligned over days, all chromatophores within a patch of skin on the last day. We then found the fraction of these chromatophores that was present on previous days within the same aligned patch. The birth rate was calculated as an exponential fit to these data, using tenfold cross-validation of skin regions. The estimated ratio of light/dark was counted from manual annotation of a patches of skin taken at high-resolution ( $n = 7$  animals). In the adult animal, light-to-dark chromatophore transition took longer than our 42-day observation period. The derivation of our model and the method used to estimate light-chromatophore lifetime are provided in full in the Supplementary Information.

**Growth model.** The model described in Fig. 6 is illustrated in more detail in Extended Data Fig. 9a. For simplicity, growth of a skin patch was modelled by a sequence of three steps, repeated every ‘day’: (1) insertion of new chromatophores; (2) isotropic expansion of skin patch; and (3) age-dependent size change of inhibitory surrounds and updating of the chromatophore-colour label. First, we explain how the inhibitory surround was constructed from observations. Second, we define the relevant parameters. Finally, we describe the simulation steps in detail and explain how parameters affect simulation outcome.

The zone of inhibition surrounding individual chromatophores in our spatial model was generated from the empirical average of chromatophore density surrounding a chromatophore ( $n=9,199$  chromatophores of both colours,  $n=1$  animal). We normalized the radial average of the density by the value of the first peak and set any value occurring at greater radial distance to 1. We then fitted a logistic function  $I(x) = \frac{1}{1 + e^{-k(x-s_0)}}$  to this density, in which  $x$  is the distance from the chromatophore centre,  $s_0$  the size (that is, distance at half-height) and  $k$  the slope at half-maximum. We inverted this function as  $1 - I(x)$ , to arrive at the one-dimensional inhibitory surround kernel (Extended Data Fig. 9d). This curve defined the radial dependence of the isotropic two-dimensional inhibitory surround  $J(\mathbf{x}) = \frac{1}{1 + e^{k(x-s_0)}}$  with vector  $\mathbf{x}=(x_1, x_2)$  denoting the two-dimensional spatial coordinates.

With the shape of the surround fixed, the simulation contained five parameters: (1) the maturation age of chromatophores (L–D transition day); (2) the rate at which chromatophores move away from each other daily (skin growth rate); (3) the size of the inhibitory surround of a chromatophore at birth ( $s_b$ ); (4) the rate of change of the inhibitory surround as a chromatophore ages ( $r_a$ ); and (5) the threshold level of skin ‘filling’ at which ‘day’ is complete. Note that these five parameters can all be varied independently of each other. Extended Data Figure 9a shows the simulation steps at which each parameter is introduced.

Our analytical growth model (above, and Supplementary Information) determines the coupling of maturation age (parameter 1), the rate of new chromatophore insertion (approximately parameter 2 squared) and the L/D ratio. We therefore fixed the values for parameter 1 and 2 approximately to values observed in a young animal and, as expected, observed a realistic L/D ratio. Parameters 3–5 determined the local spatial layout of chromatophores. Parameter 5 allowed us to model the possibility that chromatophores are not inserted to maximum packing density on any given day. Extended Data Figure 9 illustrates that this parameter affects chromatophore packing without affecting L–D interdigitation. Our results did not depend on the number of simulated ‘days’, provided that simulations were run for long enough (around 60 ‘days’) to allow L/D to reach steady state.

We defined an ‘inhibition’ field  $F(\mathbf{x})$  over the simulated patch of skin of initial size  $l \times l$  ( $l=540 \mu\text{m}$ ), in which both components of  $\mathbf{x}=(x_1, x_2)$  are real numbers in the interval  $[-\frac{l}{2}, \frac{l}{2}]$ . The inhibition field was computed as  $F(\mathbf{x}) = \sum_i J_i(\mathbf{x}-\mathbf{x}_0^i)$ , that is, by adding the inhibitory kernels  $J_i$  (see above) from all present chromatophores  $i$  with position  $\mathbf{x}_0^i$  and size  $s_0^i$  (determined by parameters 3 and 4). Values larger than 1 were set equal to 1.  $F$  was updated after every chromatophore insertion. The simulation began with an empty patch of skin, that is, with an inhibition field equal to 0 (uniform probability for chromatophore insertion). During a simulation ‘day’, chromatophores were inserted sequentially. A location was drawn from a two-dimensional uniform random distribution over the space covered by the skin patch, and insertion took place with probability  $P=1 - F$  at that location. The ‘day’ ended when no location in the inhibition field was left with a value less than the filling threshold (parameter 5). At the end of that ‘day’, the system was expanded by scaling all positions  $\mathbf{x}$  by a fixed rate (parameter 2). The size of the inhibitory surround was then adjusted according to chromatophore age ( $a$ ) as

$s_0 = s_b(1 + r_a a)$ , (until  $a=19$  days, after which  $s_0$  was fixed), and the colour of each chromatophore was updated.

We fitted parameters 3–5 to the radially averaged chromatophore-triggered densities from one animal ( $n=4,095$  dark, 5,104 light) using a grid search and mean-squared-error loss. Search space was: (3) 67–81  $\mu\text{m}$  radius (full width, half maximum); (4) –3.2% to –1.6% per ‘day’ (adjusted every two ‘days’); and (5) 0–0.5 filling threshold.

The parameters of the best fit model were (1) 19 days; (2) 2.06% per ‘day’; (3) 75.6- $\mu\text{m}$  radius (full width, half maximum); (4) –2.8% per ‘day’ (adjusted every two ‘days’); (5) 0.1. To approximate squid skin (Extended Data Fig. 10), we adjusted parameter 4 to 2.8% per ‘day’ (adjusted every two ‘days’) until 45 days of age followed by an expansion to 340  $\mu\text{m}$  radius.

**Image manipulation.** Colour images in Figs. 1c, d, 3c, 5e were uniformly and linearly scaled for clarity.

**Statistics.** Unless stated otherwise, data are mean  $\pm$  s.d. For box plots, central line indicates the median; box limits are quartiles. Whiskers extend to a maximum of  $\pm 2.7\text{s.d.}$  No statistical methods were used to predetermine sample size. The experiments were not randomized and the investigators were not blinded to allocation during experiments and outcome assessment.

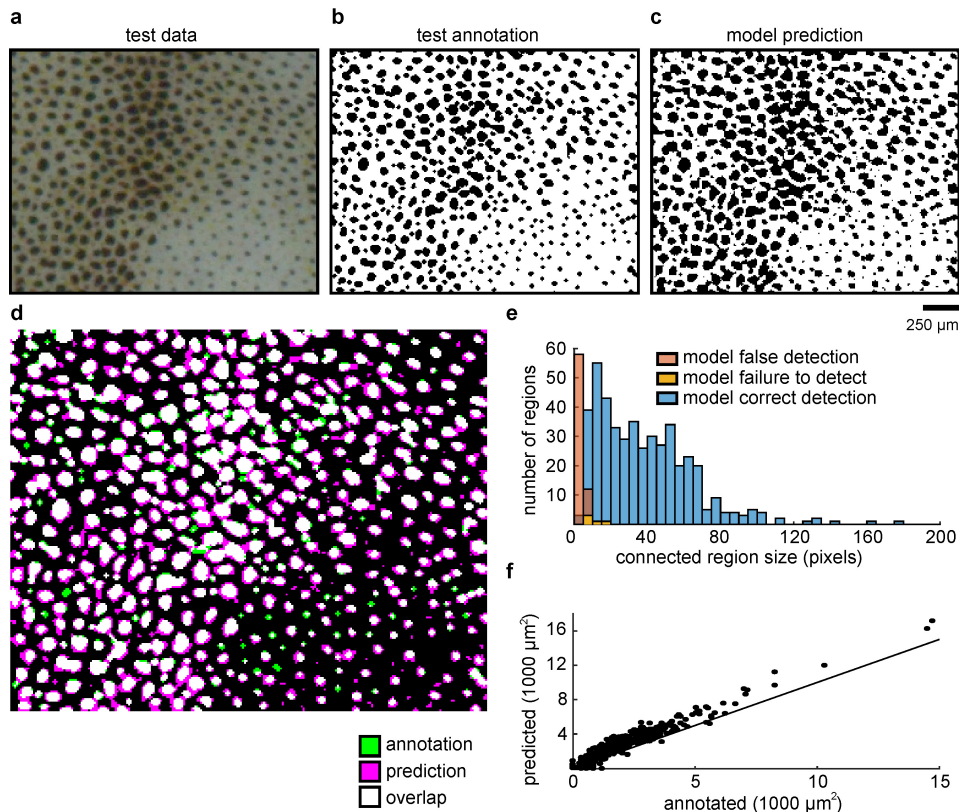
**Reporting summary.** Further information on research design is available in the Nature Research Reporting Summary linked to this paper.

**Code availability.** The code developed in this study is posted in a repository on GitHub: <https://github.molgen.mpg.de/MPIBR/cuttlefish-code-nature>.

## Data availability

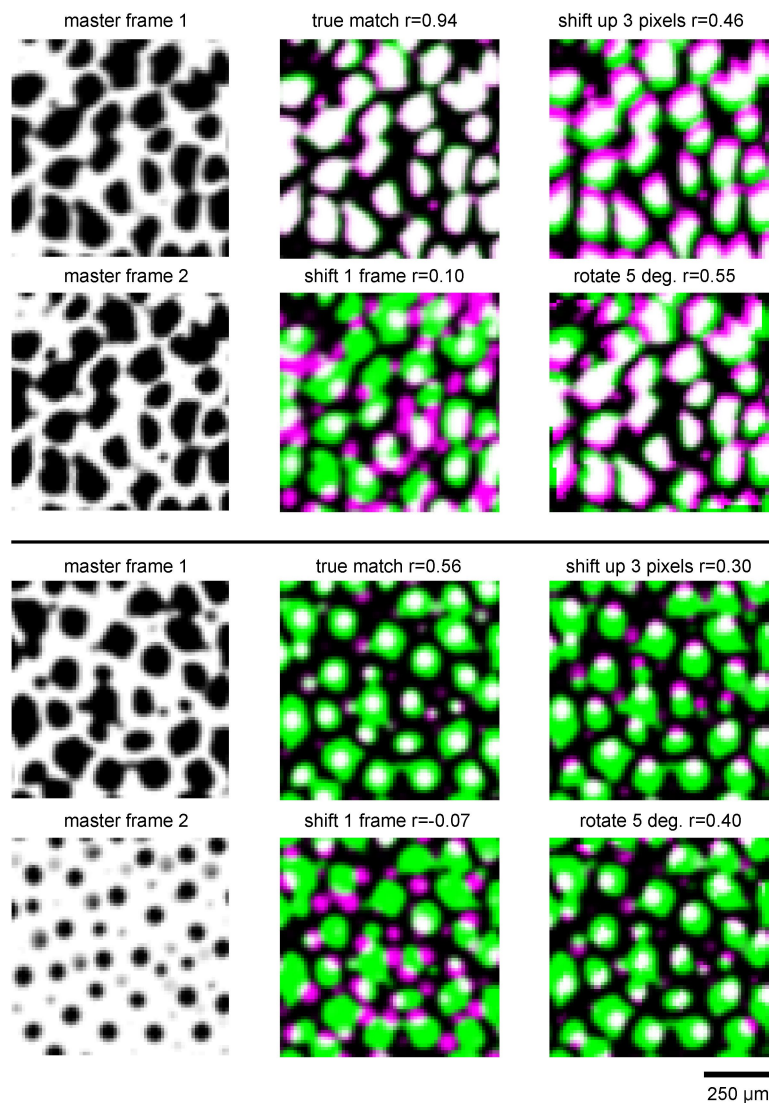
The data that support the findings of this study are available from the corresponding author upon reasonable request.

42. Butler-Struben, H. M., Brophy, S. M., Johnson, N. A. & Crook, R. J. In vivo recording of neural and behavioral correlates of anesthesia induction, reversal, and euthanasia in cephalopod molluscs. *Front. Physiol.* **9**, 109 (2018).
43. Bergstra, J., Yamins, D. & Cox, D. D. Making a science of model search: hyperparameter optimization in hundreds of dimensions for vision architectures. In *Proc. 30th International Conference on Machine Learning* Vol. 28 I-115–I-123 (Journal of Machine Learning Research, 2013).
44. Schaefer, S., McPhail, T. & Warren, J. Image deformation using moving least squares. *ACM Trans. Graph.* **25**, 533–540 (2006).
45. Fischler, M. A. & Bolles, R. C. Random sample consensus: a paradigm for model fitting with applications to image analysis and automated cartography. *Commun. ACM* **24**, 381–395 (1981).
46. Meyer, F. Topographic distance and watershed lines. *Signal Process.* **38**, 113–125 (1994).
47. Yoo, A. B., Jette, M. A. & Grondona, M. in *Job Scheduling Strategies for Parallel Processing* Vol. 2862 (eds Feitelson, D. et al.) 44–60 (Springer, Berlin, 2003).
48. Message Passing Interface Forum. MPI: a message-passing interface standard. version 3.1 <http://mpi-forum.org/mpi-31/> (2015).
49. Jones, E. et al. SciPy: open source scientific tools for Python. <http://www.scipy.org/> (2001).
50. Pedregosa, F. et al. Scikit-learn: machine learning in Python. *J. Mach. Learn. Res.* **12**, 2825–2830 (2011).
51. Walt, S. et al. scikit-image: image processing in Python. *PeerJ* **2**, e453 (2014).


**Extended Data Fig. 1 | Accuracy of the chromatophore classifier.**

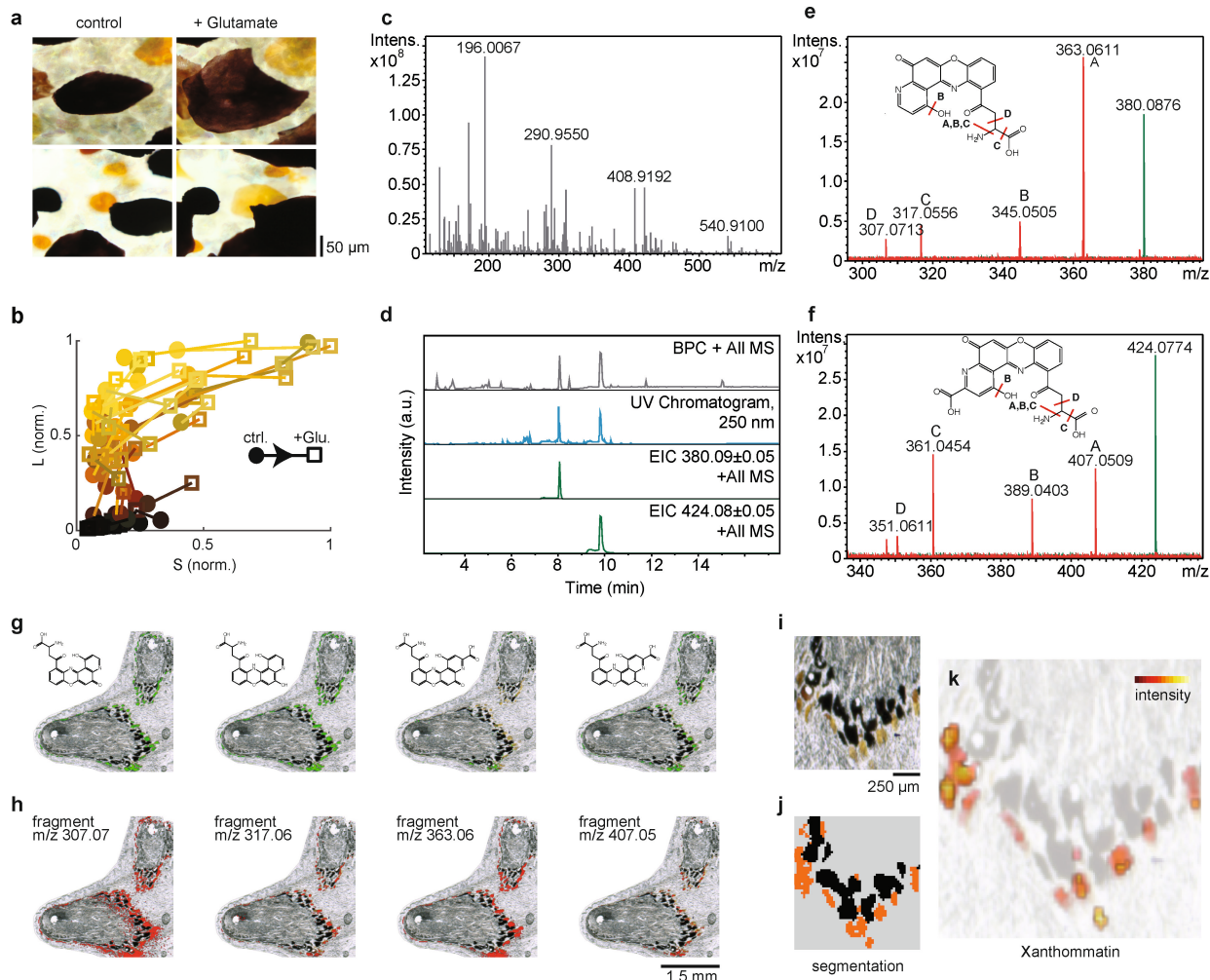
**a**, Test patch of skin used for classifier testing. **b**, Segmentation by expert human. **c**, Segmentation by classification algorithm. **d**, Composite image comparing manual (annotation) and automatic (prediction) segmentation. There was agreement for 87% of pixels, with differences mostly on the edges surrounding chromatophores. **e**, Quantification of region overlap.

Regions defined from watershedding the composite image shown in **d**. Correct detection: regions labelled by both methods. False detections: regions identified by automatic but not by manual segmentation. Failed detections: regions identified by manual but not automatic segmentation. **f**, For all regions, annotated versus predicted size. Line, identity.



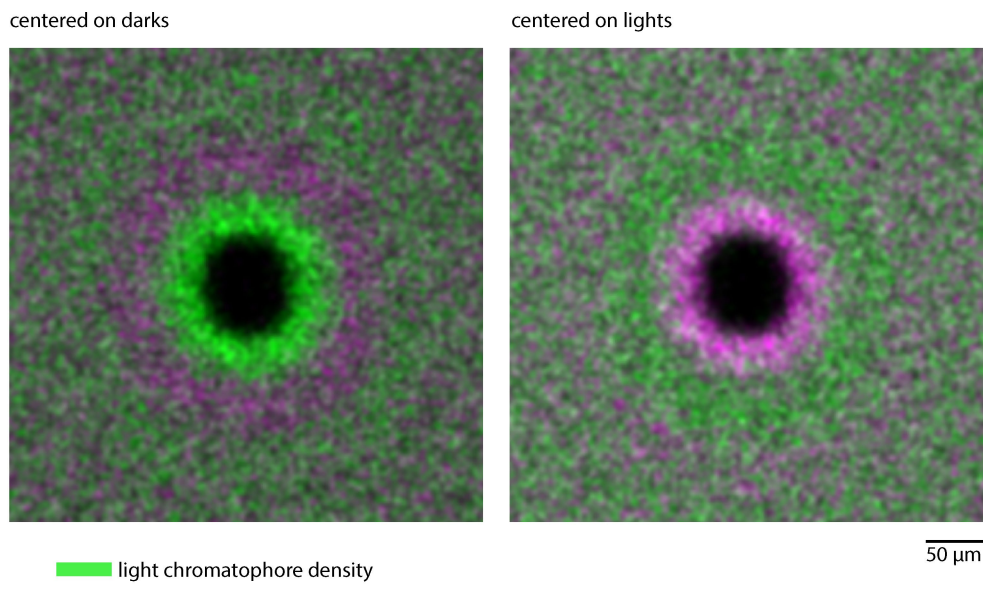
**Extended Data Fig. 2 | Sensitivity of the correlation between skin patches to small image translations and rotations.** Left, skin patches from the two sets of matching master frames shown in Fig. 1e. Middle and right, composite images of the corresponding master frames (master

frame 1 in green, master frame 2 in magenta, overlap in white). Small translations or rotations quickly lower the cross-correlation, as in the schematic in Fig. 1e, bottom.



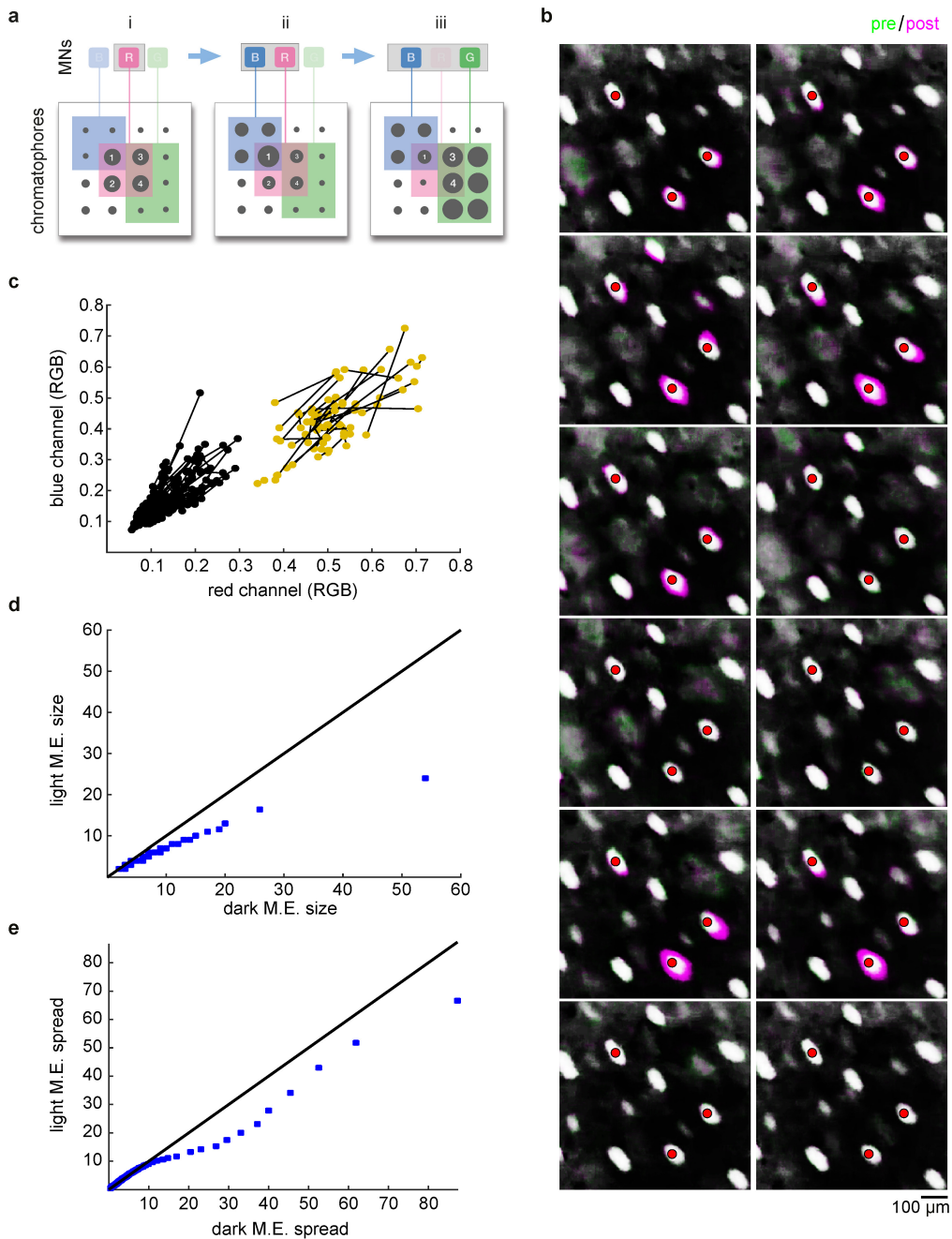
**Extended Data Fig. 3 | Identification and localization of xanthommatin in light chromatophores.** **a**, Chromatophores before (left) and after (right) local application of 40  $\mu$ M glutamate. **b**, Transmission spectra of a population of chromatophores before (circles) and after (squares) glutamate application, projected onto two dimensions defined by human L and S cone action spectra ( $n=63$  chromatophores). **c**, Direct infusion electrospray ionization Fourier-transform ion cyclotron resonance (ESI-FT-ICR) mass spectrum of the skin tissue extract showing high spectral complexity. **d**, HPLC-UV-MS chromatograms of skin tissue extract showing two main peaks with correlating ultraviolet-light (250 nm) absorption (blue) and mass spectrometry intensity (grey) consisting of eluting compounds with  $m/z$  380.09 and  $m/z$  424.08 (extracted ion chromatogram (EIC) traces, green). Experiments were replicated five times with similar results. **e**, Direct infusion ESI-FT-ICR mass spectra of skin tissue extract showing an overlay of the isolated precursor spectrum for decarboxylated xanthommatin (green,  $m/z$  380.0876, theoretical:  $m/z$  380.0877) and the fragment spectrum (red). Main fragments were assigned to putative structural losses of A (-NH<sub>3</sub>), B (-H<sub>2</sub>O, -NH<sub>3</sub>), C (-NH<sub>3</sub>, -HCOOH), D (-C<sub>2</sub>H<sub>3</sub>NO<sub>2</sub>) by accurate mass. **f**, Direct infusion ESI-FT-ICR mass spectra of skin tissue extract showing an overlay of the isolated precursor spectrum for xanthommatin (green,  $m/z$  424.0774, theoretical:  $m/z$  424.0775) and the fragment spectrum (red). Main fragments were assigned to putative structural losses of A (-NH<sub>3</sub>), B (-H<sub>2</sub>O, -NH<sub>3</sub>), C (-NH<sub>3</sub>, -HCOOH), D (-C<sub>2</sub>H<sub>3</sub>NO<sub>2</sub>) by accurate mass. **g**, Intensity distributions in laser desorption ionization Fourier-transform ion cyclotron resonance mass spectrometry (LDI-FT-ICR-MS) imaging and structures for putative xanthommatin derivatives (merged [M + H]<sup>+</sup>; [M + Na]<sup>+</sup>): decarboxylated, oxidized ( $m/z$  380.0886; 402.0696), decarboxylated, reduced ( $m/z$  382.1037; 404.0853), oxidized ( $m/z$  424.0785; 446.0629) and reduced ( $m/z$  426.0938; 448.0761). **h**, Intensity distributions of main xanthommatin and derivative fragments, corresponding to molecular species detected in ESI-FT-ICR fragmentation measurements. Experiments were performed on 12 tissue slices, producing similar results. **i**, Image of cryo-section of fresh-frozen *Sepia* skin showing chromatophores. **j**, Spatial segmentation map of section in **i**, showing distinct clusters for light and dark chromatophores (orange versus black colours) and surrounding tissue (grey). **k**, Intensity distributions for xanthommatin derivatives (merged [M + H]<sup>+</sup> and [M + Na]<sup>+</sup>) obtained from LDI-FT-ICR-MS imaging experiments ( $n=1$  sample).

an overlay of the isolated precursor spectrum for xanthommatin (green,  $m/z$  424.0774, theoretical:  $m/z$  424.0775) and the fragment spectrum (red). Main fragments were assigned to putative structural losses of A (-NH<sub>3</sub>), B (-H<sub>2</sub>O, -NH<sub>3</sub>), C (-NH<sub>3</sub>, -HCOOH), D (-C<sub>2</sub>H<sub>3</sub>NO<sub>2</sub>) by accurate mass. **g**, Intensity distributions in laser desorption ionization Fourier-transform ion cyclotron resonance mass spectrometry (LDI-FT-ICR-MS) imaging and structures for putative xanthommatin derivatives (merged [M + H]<sup>+</sup>; [M + Na]<sup>+</sup>): decarboxylated, oxidized ( $m/z$  380.0886; 402.0696), decarboxylated, reduced ( $m/z$  382.1037; 404.0853), oxidized ( $m/z$  424.0785; 446.0629) and reduced ( $m/z$  426.0938; 448.0761). **h**, Intensity distributions of main xanthommatin and derivative fragments, corresponding to molecular species detected in ESI-FT-ICR fragmentation measurements. Experiments were performed on 12 tissue slices, producing similar results. **i**, Image of cryo-section of fresh-frozen *Sepia* skin showing chromatophores. **j**, Spatial segmentation map of section in **i**, showing distinct clusters for light and dark chromatophores (orange versus black colours) and surrounding tissue (grey). **k**, Intensity distributions for xanthommatin derivatives (merged [M + H]<sup>+</sup> and [M + Na]<sup>+</sup>) obtained from LDI-FT-ICR-MS imaging experiments ( $n=1$  sample).

**Extended Data Fig. 4 | Chromatophore-centred average densities.**

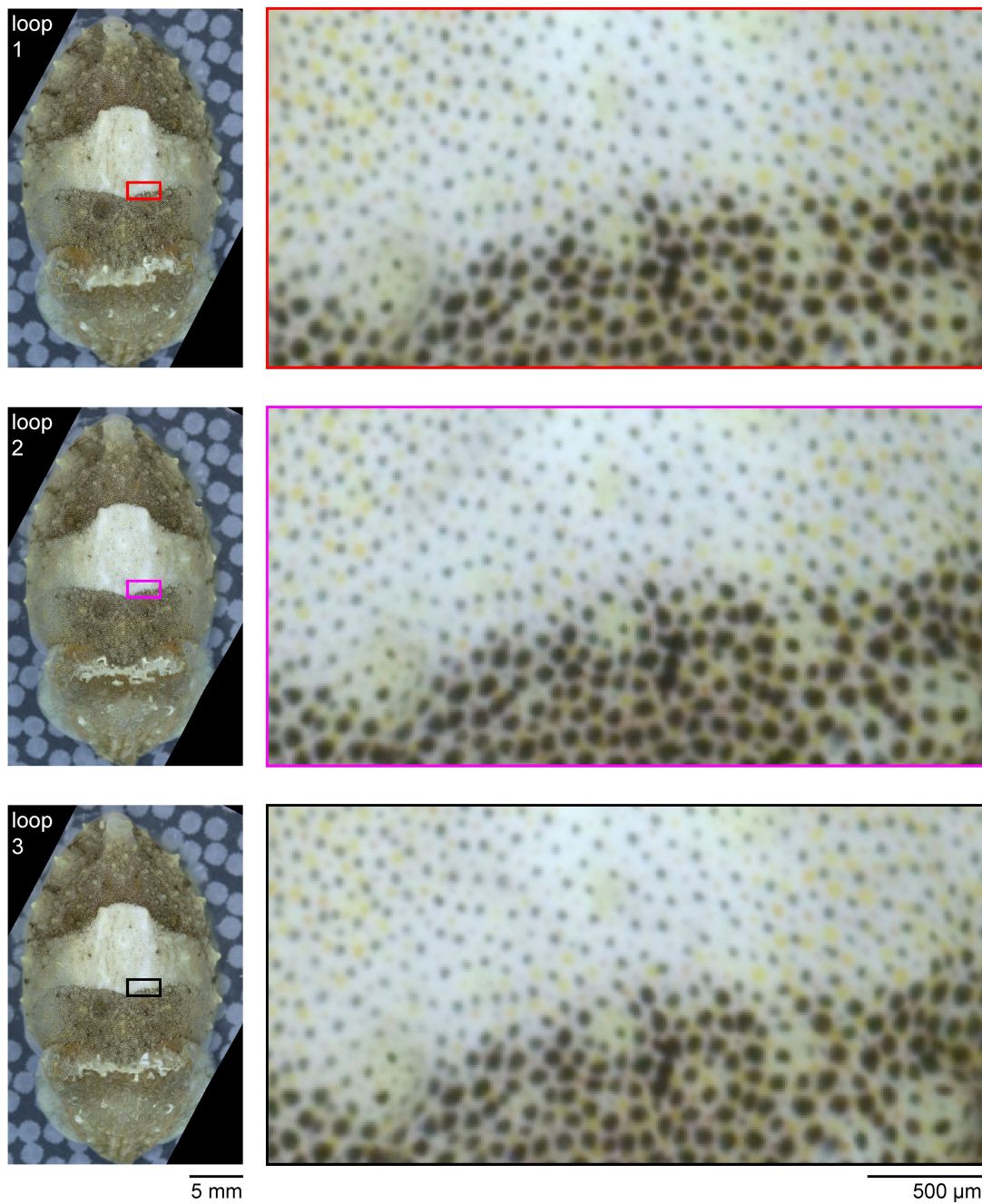
Two-dimensional density distributions for light and dark chromatophores over the mantle of an animal ( $n = 9,199$  chromatophores). The composite images show the density of light chromatophores in green and the density

of dark chromatophore in magenta. For visualization, densities were linearly scaled together within an image. This preserves relative densities within each image but leads to slightly different colours across images.



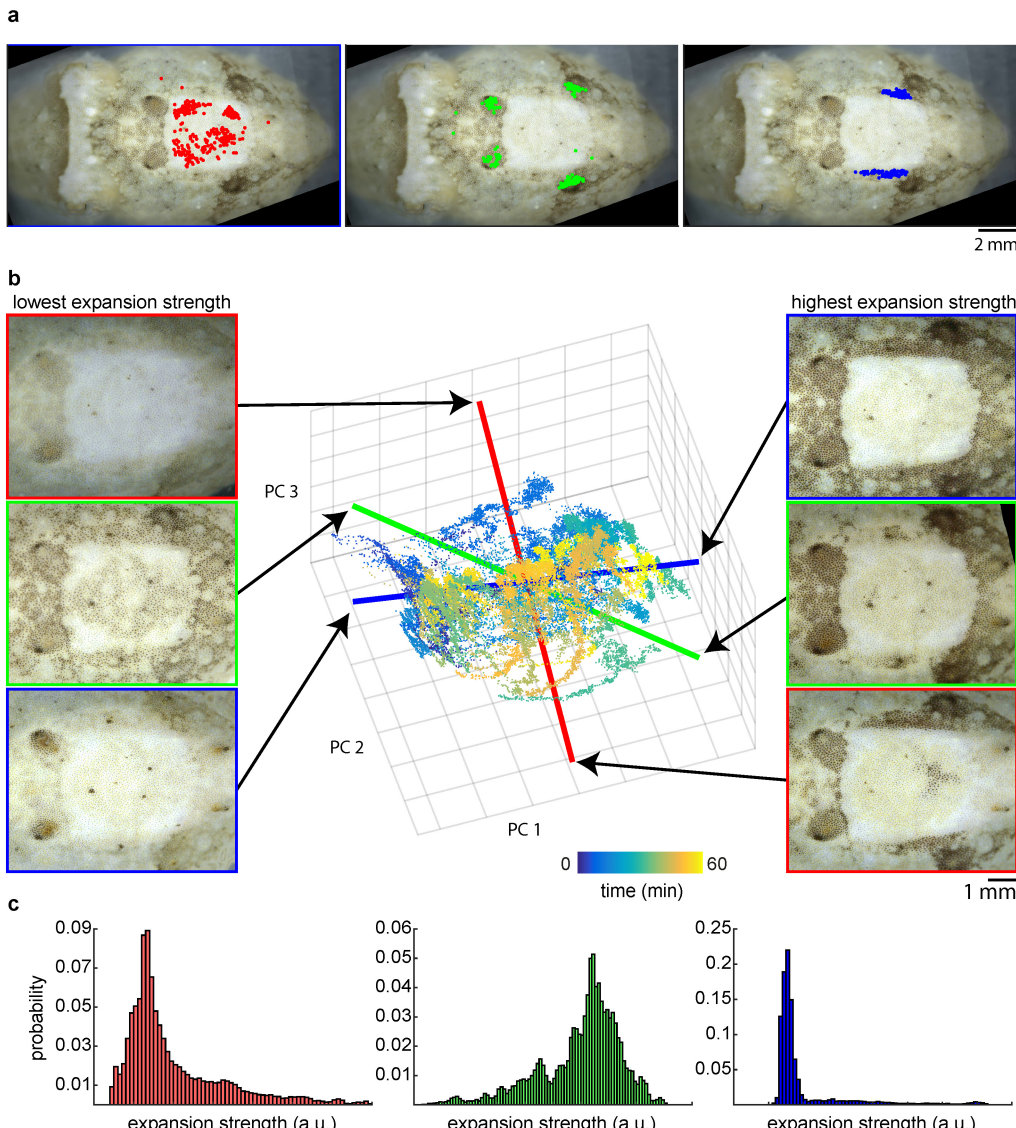
**Extended Data Fig. 5 | Identification of motor units.** **a**, Schematic showing three hypothetical, partially overlapping motor units (defined by motor neurons (MNs) B, R and G), tracked over three epochs (i–iii), each characterized by different co-activation patterns (epoch i, R alone; ii, B + R; and iii, B + G). Even though chromatophores 1–4 all belong to the same motor unit (R), their average pairwise correlation during these three epochs would differ owing to the activity of the partially overlapping motor units B and G; identifying motor units using this metric would thus fail. This hypothetical example indicates that the units of coordination during behaviour could be smaller than single anatomical motor units (they could also be larger; for example, if some motor neurons are always centrally coupled). **b**, Single trials of minimal electrical stimulation experiments in *in situ* nerves. Composite images (one per trial), green, 10 ms pre-stimulus; magenta, 200 ms post-stimulus; white, overlap.

Threshold stimulation either leads to the expansion of a set of three chromatophores (marked with red circles, for example, trial 1), or fails to activate any chromatophore (for example, trial 6, 114 motor units determined with this method). **c**, Colour assignment of chromatophores *in situ*. Colour label was assigned based on a threshold on the red channel of RGB space (0.3). Chromatophores (dots) belonging to the same motor unit (as determined in a) are connected by lines, revealing the monochromacy of motor units.  $n = 114$  chromatophores. **d**, Dark motor elements tend to be larger than light motor elements. Q–Q plot showing quantiles of the dark versus light motor element size distribution. Line, identity. **e**, Tail of distribution of motor element spread is heavier with dark than light chromatophores. Q–Q plot showing quantiles of the dark versus light motor element spread (calculated as in Fig. 3d). Line, identity.



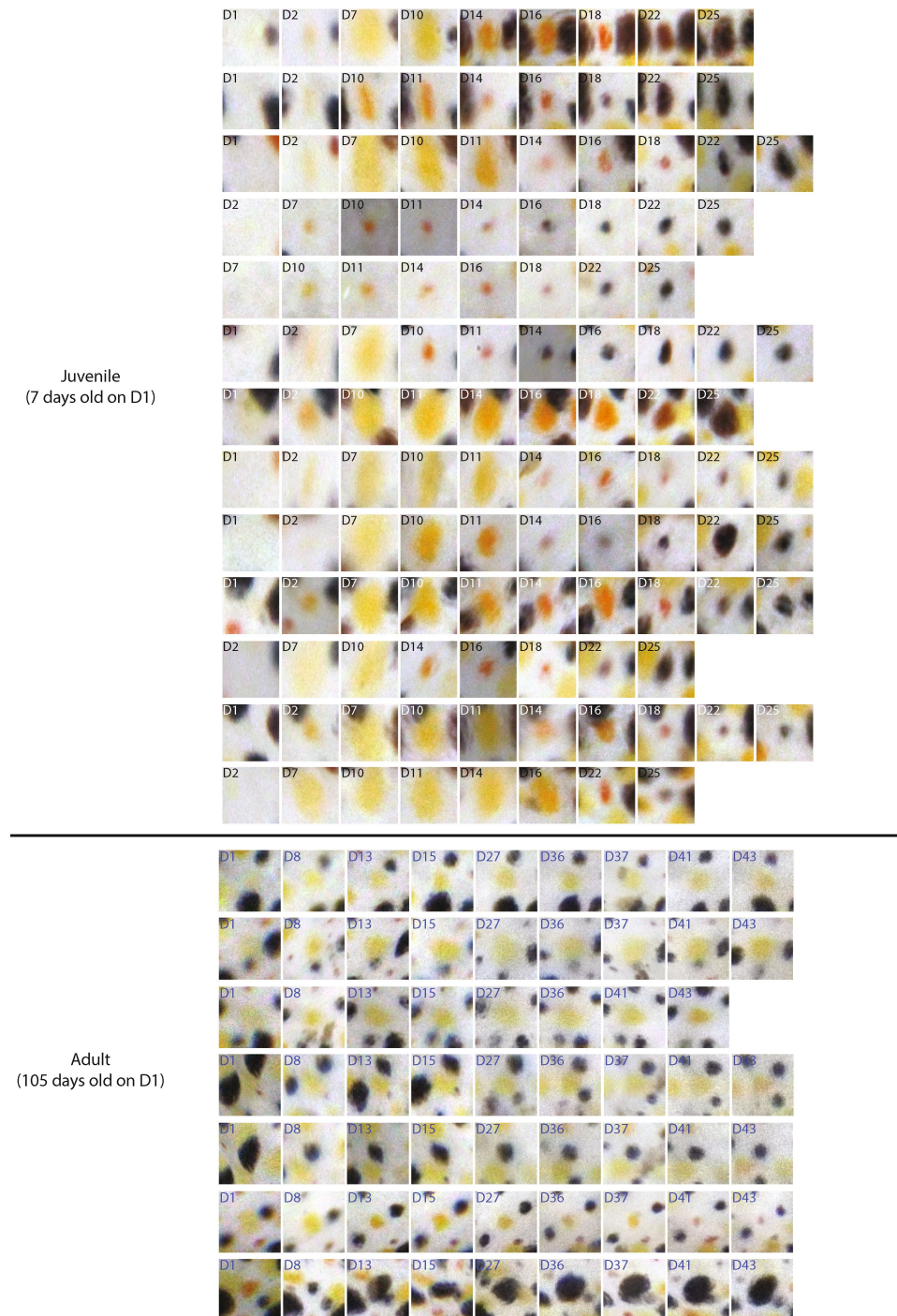
**Extended Data Fig. 6 | Pattern-border precision at single-chromatophore level.** Left, three similar points along the pattern trajectories shown in Fig. 4b after chromatophore alignment. Right, expanded view of a pattern border. Note the remarkably similar expansion

states of the chromatophores at each of the three visits, and the rugged pattern borders at chromatophore scale, with interdigitation of expanded and contracted chromatophores, generating apparent noise. This apparent noise may be critical for natural realism.



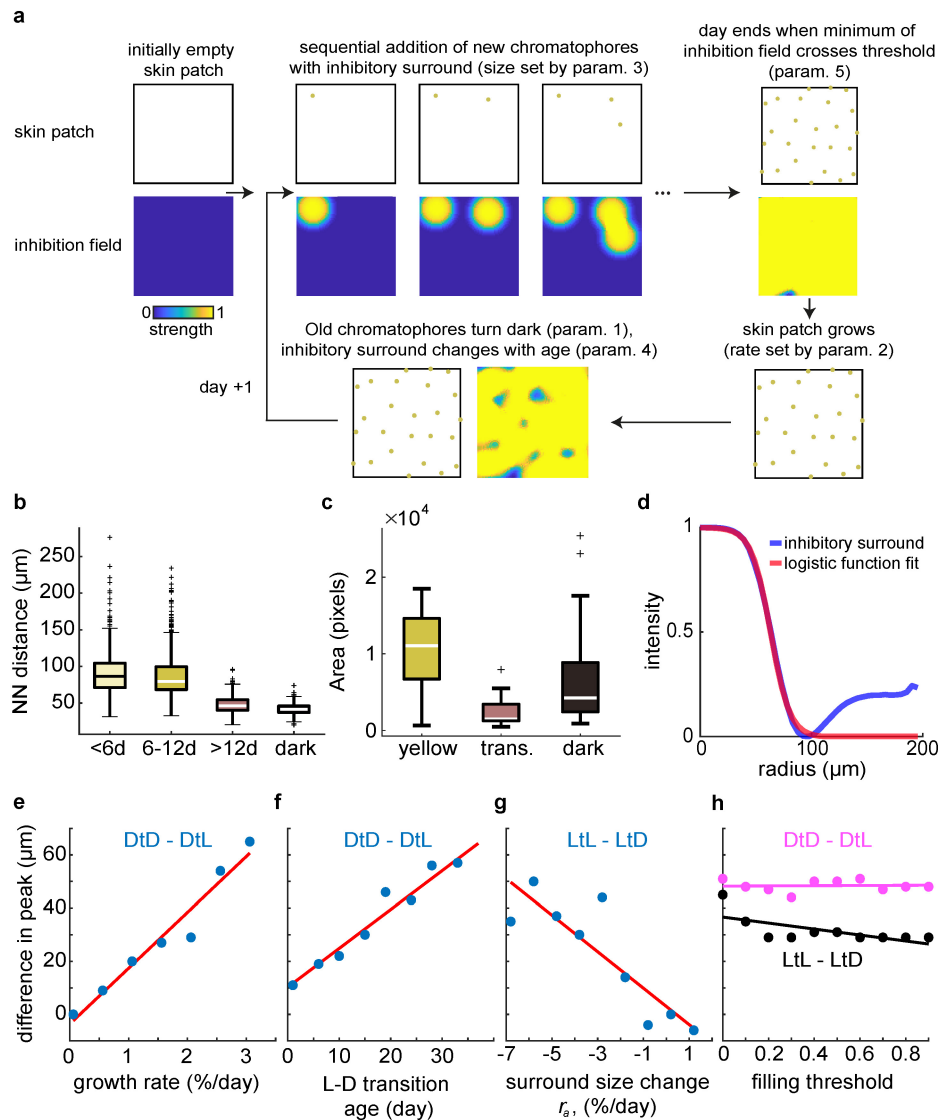
**Extended Data Fig. 7 | Linking statistical hierarchy of pattern elements to dynamics.** **a**, Three example intermediate-level clusters of motor elements (threshold of 0.4 as in Fig. 3i, different animal), overlaid on the average aligned colour image for the dataset (216,160 images). The clusters are mostly composed of chromatophores of a single colour: cluster 1 (red) is light; clusters 2 and 3 (green and blue) are dark. **b**, The dynamics of a 60-min dataset, projected onto the first three principal components (48% variance explained,  $n = 1,437$  chromatophores, 52,040 samples). A cluster activity direction can be defined in principal component space by projecting the cluster identity vector (vector of length = number

of chromatophores, with 1s assigned to chromatophores in a cluster, otherwise it is assigned 0), onto the principal components. The coloured lines show the cluster activity directions for the three clusters in a. Projecting the dataset onto these directions shows the expansion strength of the cluster at different times. The images corresponding to the times of lowest and highest strengths are shown to the left and right, respectively. c, Full distribution of expansion strengths, projecting all time points onto cluster activity directions. In this dataset, cluster 2 is often expanded, whereas clusters 1 and 3 are rarely expanded. a.u., arbitrary units.



**Extended Data Fig. 8 | Chromatophores change colour from light to dark as they age.** A gallery of aligned patches of skin centred on the position of chromatophore insertion is shown. Top, juvenile animal, 7 days old on the first day of observation (D1). Left-most column shows skin pre-chromatophore-birth. Over approximately 19 days, chromatophores that first appear pale yellow darken progressively, transitioning to orange and red, before finally turning black. Field of views (FOVs): from around

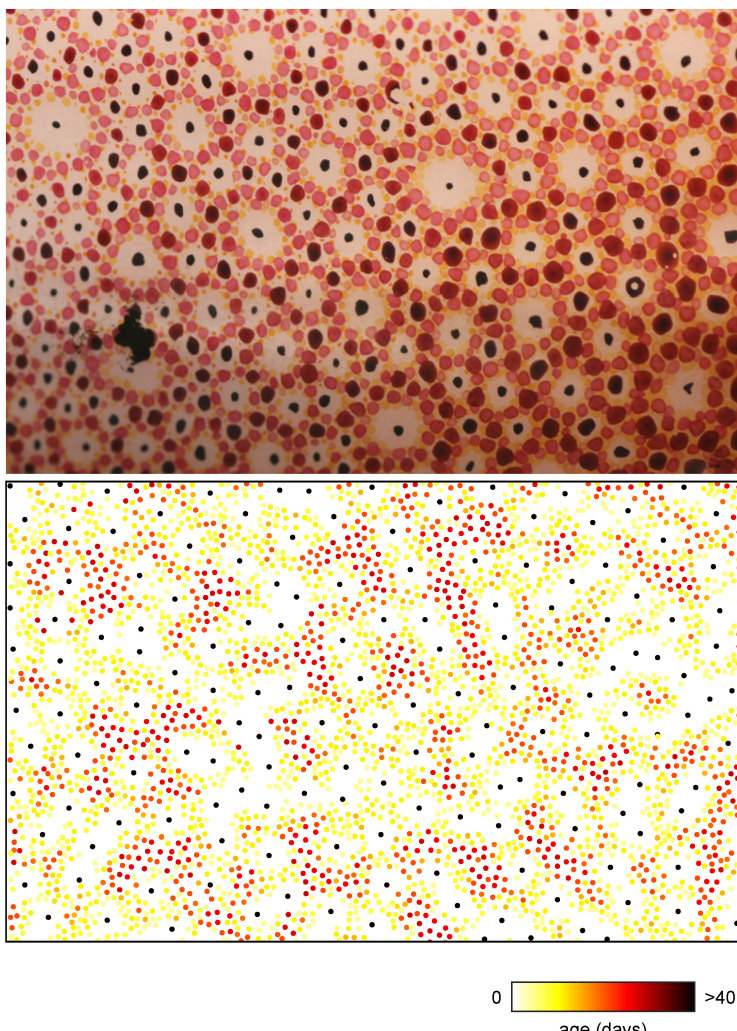
150 × 150 µm on day 1 of observation to 300 × 300 µm on day 25 of observation. Bottom, adult animal, 105 days old on day 1 of observation. Rows show chromatophores undergoing a similar light–dark colour transition as in the juvenile (top), but at a much slower rate. FOVs: around 200 × 200 µm (nonlinear alignment). Examples were chosen from aligned skin patches containing around 100 chromatophores.



#### Extended Data Fig. 9 | Development of the chromatophore array.

**a**, Flowchart depicting the spatial-growth-model algorithm and highlighting the involvement of model parameters (Methods). **b**, Box plots of nearest-neighbour (NN) distances between young (<6 days old) and older chromatophores. Young chromatophores are significantly closer to both older light (>12 days) and dark chromatophores than to other young or middle-aged (6–12 days) light chromatophores. ( $P < 0.0001$ , Kruskal–Wallis followed by Tukey's HSD,  $n_{\text{chromatophores}} = 522$  for <6 days, 541 for 6–12 days, 1,550 for >12 days, 1,910 dark chromatophores, 1 animal). Distances calculated on a single image, ages estimated by finding the day of chromatophore birth on aligned developmental datasets (Methods). **c**, Distributions of size for yellow, red (transitional (trans.)) and dark chromatophores, annotated manually (validation of analysis in Fig. 5d). Transitional chromatophores are significantly smaller than either yellow or dark ones (transitional versus yellow,  $P = 1.0 \times 10^{-7}$ ; transitional versus dark,  $P = 6.3 \times 10^{-4}$ ;  $n = 70$  yellow, 16 transitional, 84 dark chromatophores; two-tailed Wilcoxon rank-sum tests,  $n = 1$  animal). Box plots show the central line, median; box limits, quartiles; whiskers,  $\pm 2.7$  s.d. **d**, Generation of the inhibitory surround used in the skin growth model (Fig. 6b). Blue, empirical radially averaged chromatophore centred density, inverted and normalized 0:1. Red, logistic function fit to the blue density, as in Fig. 6b. **e–h**, Manipulating single parameters of the skin

growth model suggests the mechanisms underlying colour interdigitation. **e**, Difference between peak dark-triggered dark-chromatophore density (DtD) and dark-triggered light-chromatophore density (DtL), as a function of model skin growth rate. Points are from the average of three model runs. Line, linear fit. ANOVA  $F$ -statistic versus the constant model  $F = 96.6$ ,  $P = 0.000186$ . **f**, Difference between peaks of radially averaged dark-triggered dark-chromatophore density and dark-triggered light-chromatophore density, as a function of age at which chromatophores transition from light to dark. Points are from a single model run, in which the colour class was changed according to chromatophore age. Line, linear fit.  $F$ -test for linear regression:  $F = 152$ ,  $P = 5.26 \times 10^{-6}$ . **g**, Difference between first peak (first zero-crossing of derivative of radially averaged density) in the radially averaged light-triggered light-chromatophore density (LtL) and light-triggered dark-chromatophore density (LtD), as a function of  $r_a$ , the rate at which the inhibitory surround changes with chromatophore age. Points are from the average of three runs of the model. Line, linear fit.  $F$ -test for linear regression:  $F = 21.9$ ,  $P = 0.00226$ . **h**, Colour interdigitation is robust to stop-criterion used to define end of 'day' (parameter 5, Methods). Magenta, DtD – DtL (as in **e**, **f**). Black, LtL – LtD. Lines, linear fits.  $F$ -test for linear regression:  $F = 0.0206$ ,  $P = 0.889$  (DtD – DtL);  $F = 6.57$ ,  $P = 0.0334$  (LtL – LtD). Points in **e–h** are from the average of three model runs.



**Extended Data Fig. 10 | Exploration of developmental-model parameters reveals species-specific patterns.** Changing model parameters (see main text and Methods) can lead to the characteristic rings observed in some squid species, with single light chromatophores

at the centre and a radial centrifugal darkening gradient. Top, skin of common squid, *Loligo vulgaris* (image by R. Siegel). Bottom, simulation of development using a profile of change of the inhibitory disc centred on each chromatophore  $r_a$  different from that used in Fig. 6b for *S. officinalis*.

## Reporting Summary

Nature Research wishes to improve the reproducibility of the work that we publish. This form provides structure for consistency and transparency in reporting. For further information on Nature Research policies, see [Authors & Referees](#) and the [Editorial Policy Checklist](#).

### Statistical parameters

When statistical analyses are reported, confirm that the following items are present in the relevant location (e.g. figure legend, table legend, main text, or Methods section).

n/a Confirmed

- The exact sample size ( $n$ ) for each experimental group/condition, given as a discrete number and unit of measurement
- An indication of whether measurements were taken from distinct samples or whether the same sample was measured repeatedly
- The statistical test(s) used AND whether they are one- or two-sided
  - Only common tests should be described solely by name; describe more complex techniques in the Methods section.*
- A description of all covariates tested
- A description of any assumptions or corrections, such as tests of normality and adjustment for multiple comparisons
- A full description of the statistics including central tendency (e.g. means) or other basic estimates (e.g. regression coefficient) AND variation (e.g. standard deviation) or associated estimates of uncertainty (e.g. confidence intervals)
- For null hypothesis testing, the test statistic (e.g.  $F$ ,  $t$ ,  $r$ ) with confidence intervals, effect sizes, degrees of freedom and  $P$  value noted
  - Give P values as exact values whenever suitable.*
- For Bayesian analysis, information on the choice of priors and Markov chain Monte Carlo settings
- For hierarchical and complex designs, identification of the appropriate level for tests and full reporting of outcomes
- Estimates of effect sizes (e.g. Cohen's  $d$ , Pearson's  $r$ ), indicating how they were calculated
- Clearly defined error bars
  - State explicitly what error bars represent (e.g. SD, SE, CI)*

*Our web collection on [statistics for biologists](#) may be useful.*

### Software and code

Policy information about [availability of computer code](#)

Data collection

Video of behaving animals were color matched and compressed using DaVinci Resolve Studio 12.5 (Black Magic Design). In vitro experimental videos were acquired using custom software wrapping the Basler Camera SDK. MSI experiments were acquired using flexImaging 5.0 (Bruker Daltonik).

Data analysis

The main analysis pipeline in this study was written for the GNU/Linux operating system in the Python (2.7) and Cython (0.26) programming language, relying on SciPy (0.19.1), scikit-learn (0.19b2), scikit-image (0.13.0), PyQt (5.9.2), and OpenCV-Python (3.3.1). The pipeline was implemented on computing clusters, with parallel computation over steps handled by SLURM. Within a step, parallelization was achieved by spawning programs using MPI4py (2.0.0). Further data analysis was performed using custom written and code in Python and Matlab (2016a-2017b). ICA was performed using the FastICA package for MATLAB. Developmental experiments made use of the ImageJ plugin TrakEM2. MSI experiments were analyzed and visualized using SCILS Lab 2016b.

For manuscripts utilizing custom algorithms or software that are central to the research but not yet described in published literature, software must be made available to editors/reviewers upon request. We strongly encourage code deposition in a community repository (e.g. GitHub). See the Nature Research [guidelines for submitting code & software](#) for further information.

## Data

Policy information about [availability of data](#)

All manuscripts must include a [data availability statement](#). This statement should provide the following information, where applicable:

- Accession codes, unique identifiers, or web links for publicly available datasets
- A list of figures that have associated raw data
- A description of any restrictions on data availability

*Provide your data availability statement here.*

## Field-specific reporting

Please select the best fit for your research. If you are not sure, read the appropriate sections before making your selection.

Life sciences       Behavioural & social sciences       Ecological, evolutionary & environmental sciences

For a reference copy of the document with all sections, see [nature.com/authors/policies/ReportingSummary-flat.pdf](http://nature.com/authors/policies/ReportingSummary-flat.pdf)

## Life sciences study design

All studies must disclose on these points even when the disclosure is negative.

### Sample size

Image processing methods development took the form of an iterative process requiring seed data, development and testing. This loop was repeated as many times and with as many datasets as needed to converge to a performance level (99% chromatophore detection accuracy) that was deemed sufficient. Once the data analysis pipeline was developed, we analyzed data collected over many days in each animal, from six animals. Electrophysiological experiments *in vitro* were repeated until results converged to a stable variance, within the limit of available animals.

### Data exclusions

The process of data selection is explained in the text and methods sections and in Figure 1. Namely, we excluded segments of primary video data where animal movement was too brisk to enable chromatophore segmentation, as defined objectively and automatically by a quantitative measure of local contrast. Exploitable data segments were then stitched together, following the methods described in the paper (see Methods section, pipeline).

### Replication

Our study focuses in part on the development of techniques to automate data acquisition and analysis. As indicated above, the initial stages of this development required a constant loop between experiment, methods development, analysis and testing, assessment of classifier performance vs human observers, automation of analysis, and internal checks of method validity (e.g. in the spatial statistics of averaged, aligned data). After this loop converged to the levels we report, all attempted replications were successful.

### Randomization

The experiments conducted in our study were for the most part observational in nature. We made use of all animals of suitable size and, in the case of behavioral experiments, temperament. Randomization was thus not relevant for our study.

### Blinding

Investigators were not blinded to group allocation during data collection and analysis. Most experiments in our study consist of analysis of a biological system without experimental and control groups. The one exception are the experiments described in Fig. 2 c,d, in which chromatophore color is described before and after Glutamate application. In both cases, blinding was not relevant for our study.

## Reporting for specific materials, systems and methods

### Materials & experimental systems

n/a	<input checked="" type="checkbox"/> Involved in the study
<input checked="" type="checkbox"/>	<input type="checkbox"/> Unique biological materials
<input checked="" type="checkbox"/>	<input type="checkbox"/> Antibodies
<input checked="" type="checkbox"/>	<input type="checkbox"/> Eukaryotic cell lines
<input checked="" type="checkbox"/>	<input type="checkbox"/> Palaeontology
<input type="checkbox"/>	<input checked="" type="checkbox"/> Animals and other organisms
<input checked="" type="checkbox"/>	<input type="checkbox"/> Human research participants

### Methods

n/a	<input checked="" type="checkbox"/> Involved in the study
<input checked="" type="checkbox"/>	<input type="checkbox"/> ChIP-seq
<input checked="" type="checkbox"/>	<input type="checkbox"/> Flow cytometry
<input checked="" type="checkbox"/>	<input type="checkbox"/> MRI-based neuroimaging

## Animals and other organisms

Policy information about [studies involving animals](#); [ARRIVE guidelines](#) recommended for reporting animal research

Laboratory animals

European cuttlefish *Sepia officinalis* were hatched from eggs collected in the English Channel and reared in a closed seawater system. Animals of both sexes, 1 day - 40 weeks old, were used in this study.

Wild animals

This study did not involve wild animals.

Field-collected samples

This study did not involve field-collected samples.